Automatic Detection of Local Obstacles in Long Length High Temperature Superconducting REBCO Coated Conductors by Deep Learning Based Image Analysis in Reel-to-Reel Magnetic Microscopy

ソムジャイジャルン, ナタウィロー

https://hdl.handle.net/2324/5068237

Automatic Detection of Local Obstacles in Long Length High Temperature Superconducting REBCO Coated Conductors by Deep Learning Based Image Analysis in Reel-to-Reel Magnetic Microscopy

Natthawirot Somjaijaroen

2022

Automatic Detection of Local Obstacles in Long Length High Temperature Superconducting REBCO Coated Conductors by Deep Learning Based Image Analysis in Reel-to-Reel Magnetic Microscopy

By

Natthawirot Somjaijaroen

A thesis submitted to Kyushu University

for the degree of Doctor of Engineering

Department of Electrical and Electronic Engineering

Graduate School of Information Science and Electrical Engineering

Kyushu University

Fukuoka, Japan

September 2022

Abstract

The importance of spatial uniformity of local critical current, I_c, in long length high-temperature superconducting tapes has been increasingly recognized in recent years from the viewpoint of reliability and stability of the applied equipment as a required specification. The uniformity of local I_c along the CCs was usually restricted due to any local obstacles that occurred during the long fabrication process. Usually, the I_c along the CCs was limited due to obstacles and characterized by one-directional characterization, TAPESTAR. It measures I_c variation as a function of longitudinal coordinate and identifies I_c drops for ensuring uniformity in long CCs, but the measurement does not give sufficient information to study local obstacles in more detail due to a lack of spatial resolution along the tape width direction. However, the Reel-to-Reel Scanning Hall-probe Microscopy (RTR-SHPM) is possible to visualize inhomogeneity on two-dimensional magnetization current distribution because of its high resolution across the tape width. Based on this approach, it has been utilized to introduce deep learning-based based image analysis, such as classification and object detection to analyze the inhomogeneity in the long tape of several hundreds of meters because it still requires so much time to analyze the result of RTR-SHPM for whole length by the human eye in order for characterizing detailed features of the obstacles such as shape, size and position. Moreover, the inhomogeneity of commercial HTS coated conductors made from different fabrication processes is extended by adopting the deep learning-based based image analysis to recognize the local obstacle and to extract not only merely the critical current, I_c value, but also more detailed information on local current limiting factors such as the types of local obstacle in each coated conductor tapes, the influence of fabrication processes, statistical properties of local defects and its influence on the positional local critical current over the defect region even under the influence of intrinsic fluctuation of I_c in the normal region, which are difficult to detect by the conventional characterization. Hence, the instant characterization or analytical techniques is essential for the evaluation and provide such helpful information leading further research and development of the REBCO.

Contents

Chapter 4

Further upgrade the performance of the image classification

Chapter 5

Object detection for recognizing defect in HTS tapes   66

Chapter 6

Image pixel interpolation for image recognition   79

Chapter 7

Conclusion   84

Chapter 1

Introduction

1.1 Background

1.1.1 High temperature superconductors (HTSs)

Superconductivity is a phenomenon of the zero electrical resistivity of materials when they are cooled to sufficiently low temperature called critical temperature (T_c). This phenomenon was first discovered in 1911 by the Dutch physicist H. Kamerlingh Onnes and his assistant Gilles Holst in Leiden. They found that the dc resistivity of mercury suddenly dropped to zero when the temperature was dropped to below 4.2 K, so this material transformed from the normal conducting state to the superconducting state for the first time. In the superconducting state, the electrons that carry the current are not scattered by the atoms/ions, resulting in dissipation due to thermal motion. Since this motion is reduced with decreasing temperature, the electrical resistance is also reduced [1, 2].

In 1986, the high-temperature superconductivity (HTS) in a perovskite structured lanthanum based cuprate oxide ($La_{2-X} Ba_X CuO_4$) with a critical temperature of 35 K was first discovered by Georg Bednorz and Karl Müller [3]. The range of this transition temperature best confirmed at present extends from 90 K for the replacement of La by Y for the compound $YBa_2Cu_3O_7$ was discovered by M. K. Wu, P. W. Chu and his students at the University of Alabama, Huntsville in 1987 [4]. Many researchers have ever investigated the HTSs, including the crystal structure of $Bi_2Ca_2Sr_2Cu_3O_x$ with $T_c > 110$ K, which H. Maeda proposed in 1987 [5]. These were usually called type-II superconductors and a remarkable discovery to push the transition temperatures well beyond the liquid nitrogen temperature (77 K), which is a much cheaper and easily accessible medium than liquid helium. The development of T_c for various conventional and high-temperature superconductors as a function of the year of their discovery is shown in Fig. 1.1.
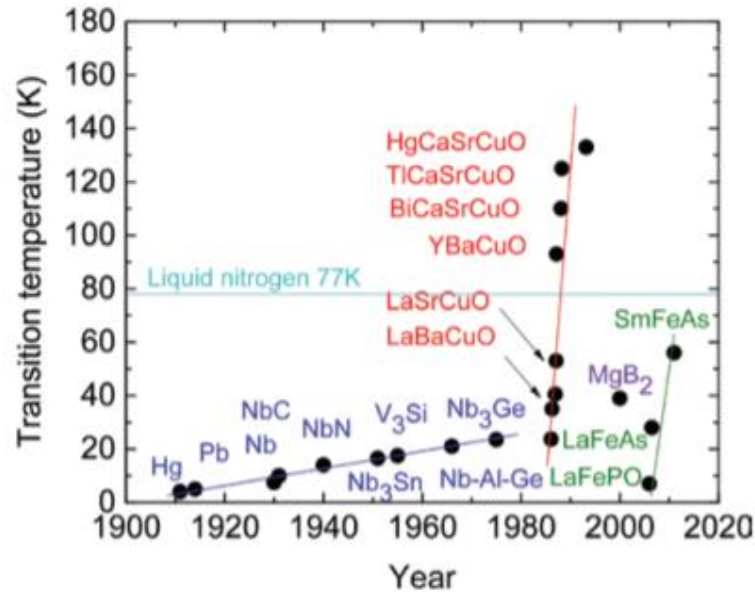
Fig. 1.1 The development of T_c for various conventional and high-temperature superconductors as a function of the year of their discovery [6]

1.1.2 The architecture of high-temperature superconductors

The high-temperature superconductivity has a chemical composition of $REBa_2Cu_3O_x$ (Rare-earth barium copper oxide, REBCO). The crystal structure of the REBCO superconductor is shown in Fig. 1.2. The CuO_2 layers are separated by insulating layers and exist superconducting current in its ab-plane.
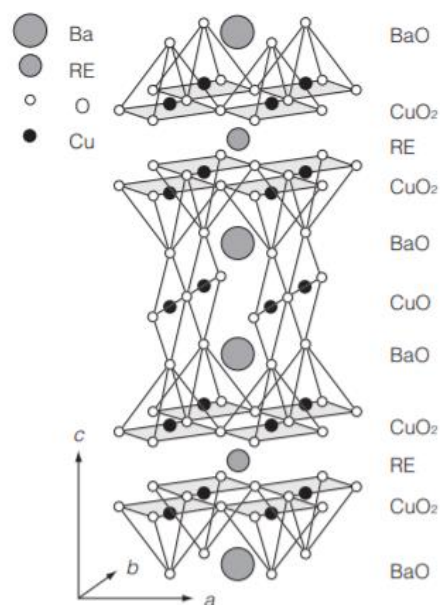
Fig. 1.2 The crystal structure of REBCO superconductor [7]

In 1988, The high J_c (10^3-10^4A/cm^2) was succeeded in epitaxial YBCO films deposited on single crystalline oxide substrates (MgO, STO) [8]. The film aligned in c-axis normal to substrates (out-of-plane) was still randomly distributed high-angle grain boundaries in the ab-planes resulting in suppressing critical current density. The method to solve this problem is to deposit both in-plane and out-of-plane texturing of the superconducting layers on buffered metal substrates in a biaxial alignment. It requires biaxially alignment like a single crystal along the long tape [9]. Therefore, the superconducting properties of REBCO coated conductors mainly depend on two common layers: a biaxially aligned polycrystalline buffer layer on the substrate and an epitaxial REBCO layer.

In order to obtain in-plane grain alignment of buffer layer crystals on a metallic substrate, there were two approaches employed: ion beam-assisted deposition (IBAD) [10] and rolling-assisted biaxially textured substrates (RABiTS) [11]. Architecture of coated conductors based IBAD and RABiTS is shown in Fig. 1.3.
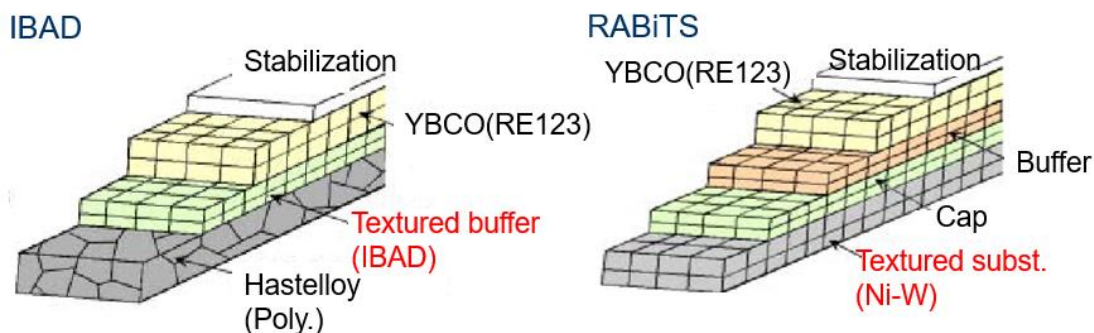
Fig 1.3 Architecture of coated conductors based IBAD and RABiTS [12]

In 1991, the bi-axially aligned polycrystalline buffer layer on the non-textured metal substrate was succeed in introducing of IBAD process that developed by Ar+ ion beam irradiated from a particular angle and the epitaxial REBCO layer was deposited on this bi-axially aligned polycrystalline buffer layer using pulsed laser deposition (PLD). As a result, The J_c was more 10^5 A/cm^2 on the metal substrate [13]. The IBAD process is displayed in Fig. 1.4. In the case of RABiTS, biaxial texturing is carried out through cold rolling and recrystallization of the metallic substrate (Ni). This process of

biaxially oriented buffer layer on the polycrystalline metallic substrate is deposited before the deposition of the superconducting film.
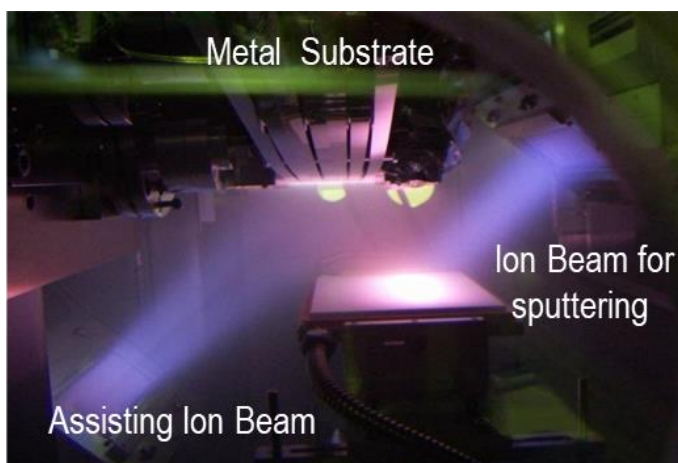
Fig. 1.4 IBAD process [14]

However, many groups of researchers have also developed the deposition of superconducting layer on this biaxially oriented buffer layer to achieve high current density in high magnetic field and scale up this process for long lengths coated conductors. Nowadays, the epitaxial superconducting layer is deposited by at least four deposition techniques by chemical routes, such as metal-organic deposition (MOD) [15] and metal organic chemical vapor deposition (MOCVD) [16], or by physical routes, such as pulsed laser deposition (PLD) [17] and reactive co-evaporation (RCE) [18]. The schematic of each technique is shown in Fig. 1.5.
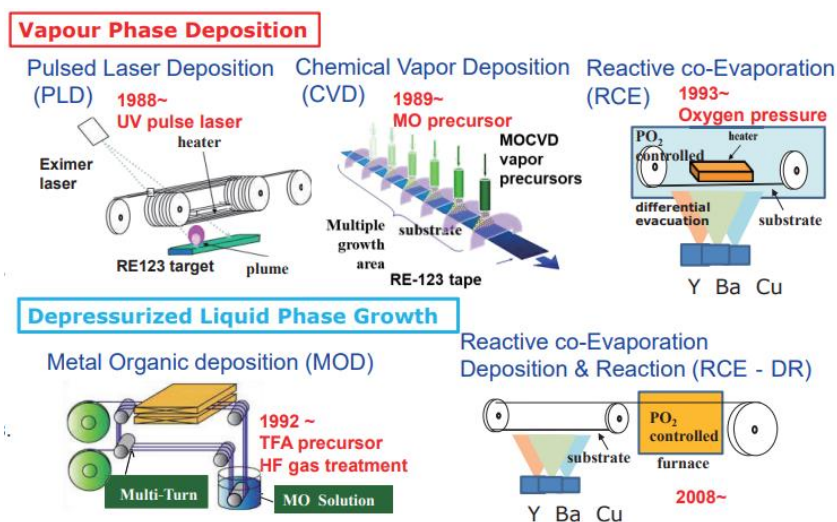
Fig. 1.5 Development of REBCO film formation techniques [19]

The development of HTS coated conductors with different fabrications, conductor architecture and materials were driven by various manufacturers, namely Fujikura Ltd (Japan), SuNAM Co. Ltd (Korea), SuperOx ZAO (Russia), SuperPower Inc. (US) etc. The example of a schematic of the structure of REBCO tapes made from Fujikura Ltd. is shown in Fig. 1.6. They consists of a subtract, buffer layer, superconducting layer, and other stabilizing layers. The CCs can be manufactured in flexible, long lengths using IBAD-PLD process. Based on these properties and their superior critical current properties under high magnetic fields, they are expected to be applied for many applications such as power cables, magnetic resonance imaging (MRI), reactors, and other various electrical applications, as shown in Fig. 1.7 [20].
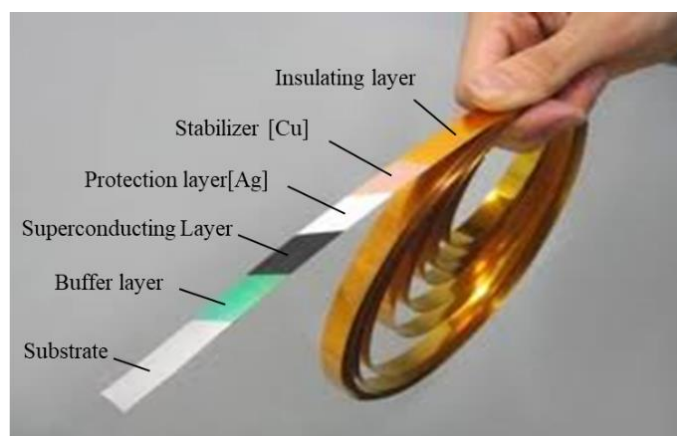
Fig. 1.6 Schematic of RE-based HTS tape [21]
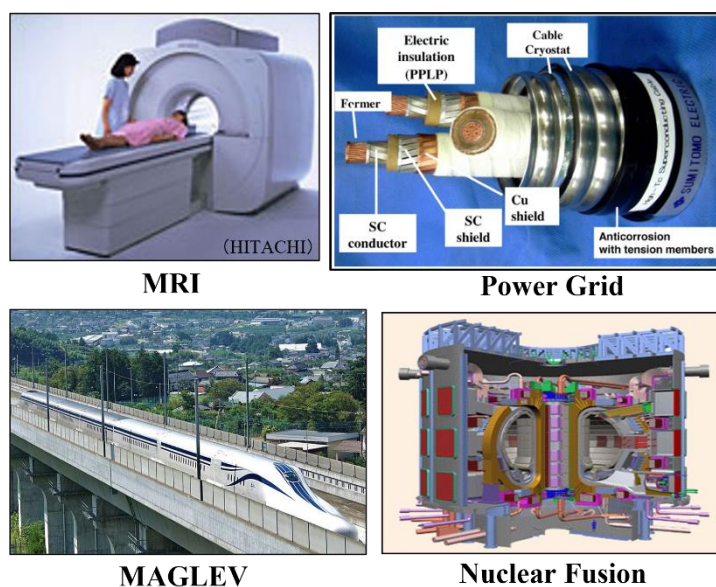
Fig. 1.7 HTS applications [22-25]

1.1.3 The evaluations of HTS tapes

The further optimization in the HTS fabrication process is still required to improve not only the long length of tapes but also the non-uniformity of critical current (I_c) along the length, which are so important for the high performance of practical applications. The non-uniformity of superconducting properties is the main critical issue and can result from undesired structural damage, macroscopic defect, contamination, and impurities during the long length manufacturing process and originate from multiple layers of the CCs [26-28].

The inhomogeneity normally affects the local critical current (I_c) along the longitudinal direction of the tapes so the conventional characterization such as TAPESTAR™ [29] is used for evaluating I_c value as a function of longitudinal coordinate, shown in Fig 1.8. It is used as a de facto standard method which can indicate the significant I_c drops caused by local defects. However, the lack of spatial resolution across the tape width makes it difficult to visualize defects in two-dimensional (2D), which can study more in detail. Reel-to-reel Scanning Hall-probe microscopy (RTR-SHPM) [30], [31] has been a promising measurement using scanning Hall-probe with high spatial resolution across the width direction as well as the longitudinal direction. It measures the distribution of the magnetic fields above the sample in a remanent state with a non-destructive and contactless system. By considering the inversion problem of Biot-Savart law, the critical current density (J_c) was estimated from the corresponding magnetic field distributions. The advantage of this method can provide information about 2D J_c mapping along the tapes and characterize the local defect by checking the in-plane J_c distributions, as shown in Fig. 1.9.
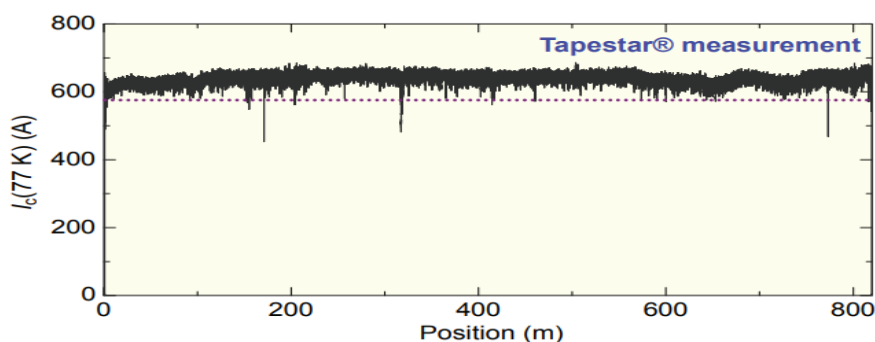
Fig. 1.8 Longitudinal distributions of critical currents in a tape characterized by the conventional technique: TAPESTAR [32]

Sheet current density $|J_c|$ (A/mm)
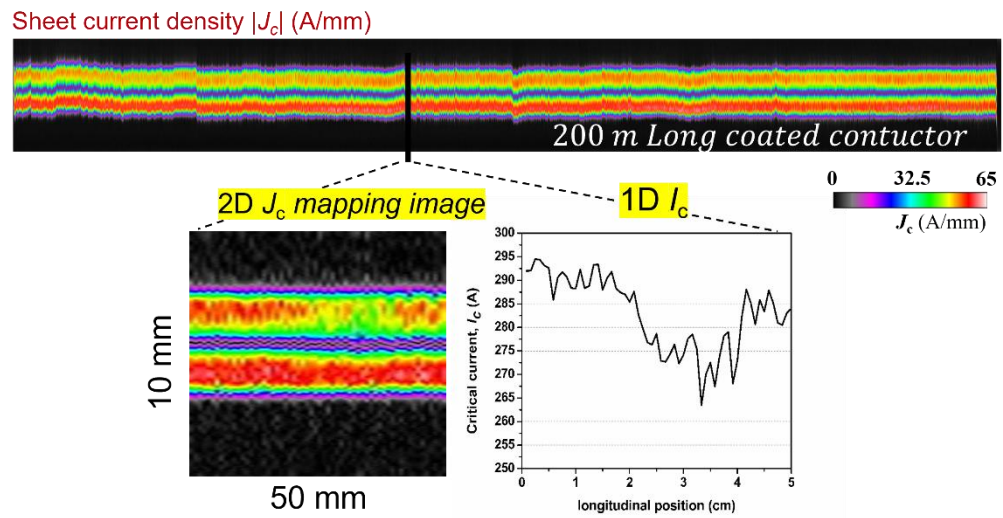
Fig. 1.9 The current density distribution in a long REBCO coated conductor characterized by RTR-SHPM.

1.2 Research purpose

As mentioned above, the non-uniformity along the long tapes is a key issue for the high performance of practical applications. Because the mass production of CCs in many companies has been fabricated on a scale of several hundreds of meters, the instant characterization or analytical techniques is essential for the evaluation and provide such helpful information for the improvement of the REBCO. Not only merely the critical current, I_c value, but also more advanced information of obstacles is required for the research and development.

Currently, many deep learning algorithms have been used to accelerate and solve various challenges of big data [33], [34]. One of the most remarkable candidates dealing with various kinds of images and object in image is image recognition, such as image classification and object detection [35]. In this research, we integrated high-resolution 2D characterization: RTR-SHPM with deep learning-based image analysis for automatically evaluating more detailed information on local obstacles in the long length CCs.

Chapter 2

Characterization method of HTS tapes

The superconductors are able to transfer large currents through a long length of superconductor without electrical resistance or dissipation. This maximum value is called the critical current (I_c). Hence, the estimation of the longitudinal distribution of the critical current is a basic indicator for characterizing long superconductors. Characterization methods of a superconductor are performed by either measuring the one-dimensional distribution of critical current or two-dimensional distribution of current density distribution (J_c), which is the critical current per unit cross-sectional area of the superconductor. The methods, namely RTR-SHPM and Tapestar^{TM} system are described for evaluating the superconducting properties in this chapter.

2.1 RTR-SHPM system

2.1.1 Principle of RTR-SHPM

In this research, we use RTR-SHPM to characterize the long tapes, as shown in Fig 2.1. Because high spatial resolution measurements across the width direction as well as the longitudinal direction, the RTR-SHPM characterization can fully visualize a two-dimensional (2D) inhomogeneity with a non-contact or non-destructive manner. While the long tape was traveling under a liquid nitrogen container in the longitudinal direction from transport feeding reel to retrieval reel and passed the external magnetic field, then 2D distribution of the magnetic fields above the sample surface in a remanent state was measured continuously by scanning a Hall sensor at high speed across the width direction [30], [31]. The schematic of RTR-SHPM system is shown in Fig 2.2. The spatial resolution was 833 µm and 20 µm in longitudinal and width directions, respectively.

Fig. 2.1 RTR-SHPM system [36]
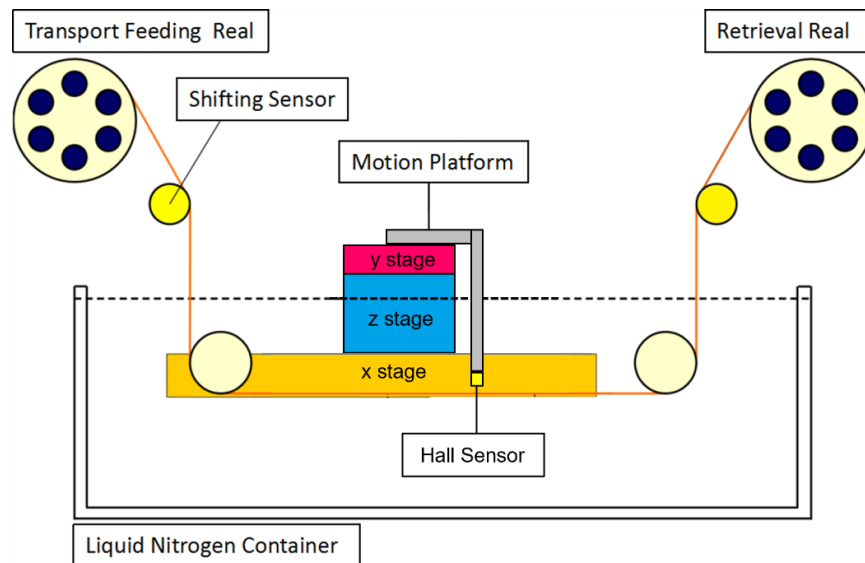
Fig. 2.2 Schematic of RTR-SHPM system

The system can measure the magnetic penetration after being magnetized until the full flux penetration. According to Meissner effect, whenever a superconductor is placed in a weak external magnetic field and cooled below its critical temperature T_c, the magnetic field is ejected in Fig. 2.3. It does penetrate the superconductor due to also small shielding current be generated to prevent the magnetic flux. As the external magnetic field increases, more magnetic field penetrates the inside of the superconductor, and the shielding current begins to flow and shield such the external magnetic field, Fig. 2.4. When the external magnetic field is sufficiently applied until

the shielding current flows in the center of the conductor and is then removed, the shielding current continues to flow in the opposite direction from the applied magnetic field. Then, the shielding current flowing at the amplitude of critical current density J_c is shown in Fig 2.5. According to Lenz's law, when a changing magnetic field is applied to a conductor, it will induce an electric current in the conductor creating an opposing magnetic field, even the external magnetic field disappear, the inverse electric current also creates an opposing magnetic field. This opposing magnetic field can be measured by Hall prob of RTR-SHPM system. Then, this corresponding critical current density can be calculated by solving inverted Biot-Savart law.

Fig. 2.3 Shielding current generated by magnetic field [36]
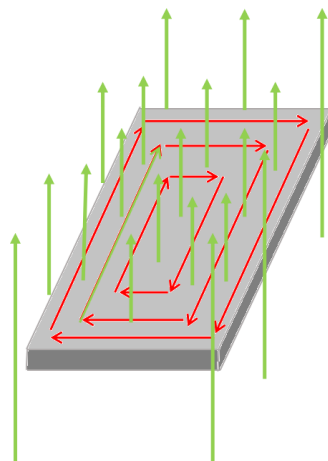
Fig. 2.4 Shielding current generated by high magnetic field [36]
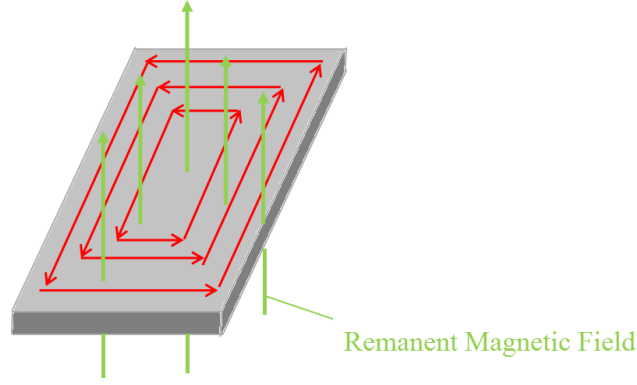
Fig. 2.5 Shielding current after initial magnetization [36]

2.1.2 Evaluation of current density distribution [31], [37]

The Biot–Savart law is a physics equation that describes the magnetic field produced by an electric current. It connects the magnetic field to the magnitude, direction, length, and proximity of the electric current. The magnetic field can be used to determine the electric current using the inverse Biot-Savart law.
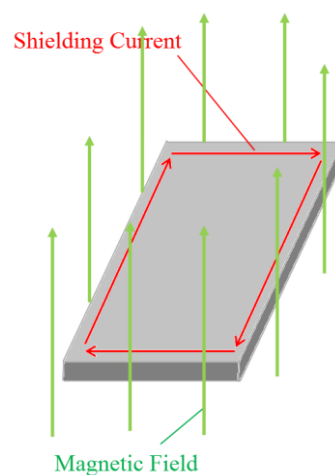
Biot-Savart Law equation in SI unit is described by the following equation.

$$\boldsymbol{B}(\boldsymbol{r}) = \frac{\mu_0}{4\pi} \int \frac{\boldsymbol{J}_{\mathrm{d}}(\boldsymbol{r}')\times(\boldsymbol{r}-\boldsymbol{r}')}{|\boldsymbol{r}-\boldsymbol{r}'|^3} d\boldsymbol{r}' \tag{2.1}$$

$\boldsymbol{B}(\boldsymbol{r})$ is resultant magnetic field $\boldsymbol{B}$ at position $\boldsymbol{r}$ created by a steady current density $\boldsymbol{J}_{\mathrm{d}}$ at position $\boldsymbol{r}'$, μ_0 is the magnetic permeability in a vacuum. By Eq. (2.1), the current density $\boldsymbol{J}_{\mathrm{d}}$ also can be solved by $\boldsymbol{B}(\boldsymbol{r})$. When comparing the 2D and 3D equations for computing current density $\boldsymbol{J}_{\mathrm{d}}$ by $\boldsymbol{B}(\boldsymbol{r})$, the 3D calculation is much more complicated. The uniform $\boldsymbol{J}_{\mathrm{d}}$ can be considered two-dimensional in the x-y plane where $z = 0$. It is assumed that a current density $\boldsymbol{J}_{\mathrm{d}}$ lies wholly in a thin sheet and that the thickness can be ignored. Furthermore, we assume that the current is quasistatic so that the inverse problem can be solved by 2D equation. The x component of magnetic field generated by current density J_y at measurement position $\boldsymbol{r}$ (x, y, z) is expressed by the following equation.

$$B_x(x, y, z) = \frac{\mu_0 z}{4\pi} \int \int \frac{J_y(x',y')}{((x-x')^2+(y-y')^2+z^2)^{\frac{3}{2}}} dx'dy' \tag{2.2}$$

Eq. (2.2) represents a convolution of the current density $J_y(x', y')$ with a weighting function, or Green's function, that depends only on the distance between r and r'. The convolution theorem allows us to write this equation as the following equation.

$$b_x(k_x, k_y, z) = g(k_x, k_y, z)j_y(k_x, k_y) \tag{2.3}$$

In Eq. (2.3), $b_x(k_x, k_y, z)$ and $j_y(k_x, k_y)$ are the two-dimensional Fourier transforms of the magnetic field and current density, respectively. $g(k_x, k_y, z)$ is the Fourier transform of the Green's function:

$$G(x - x', y - y', z) = \frac{\mu_0}{4\pi} \frac{z}{((x-x')^2 + (y-y')^2 + z^2)^{\frac{3}{2}}} \tag{2.4}$$

The two-dimensional Fourier transform is defined as

$$j_y(k_x, k_y) = \iint J_y(x', y') e^{-i(k_x x' + k_y y')} dx' dy' \tag{2.5}$$

to give the inverse Fourier transform given by

$$J_y(x, y) = \frac{1}{(2\pi)^2} \iint j_y(k_x, k_y) \times e^{-i(k_x x' + k_y y')} dk_x dk_y. \tag{2.6}$$

The variables k_x and k_y are the components of the spatial frequency k. The transform of the expression in Eq. (2.4) can be evaluated analytically and is obtained by the following equation.

$$g(k_x, k_y, z) = \frac{\mu_0}{2} e^{-\sqrt{k_x^2 + k_y^2}} \tag{2.7}$$

Similarly, we can calculate the y and z components of the magnetic field:

$$b_y(k_x, k_y, z) = \frac{\mu_0}{2} e^{-kz} j_x(k_x, k_y), \tag{2.8}$$

and

$$b_z(k_x, k_y, z) = i \frac{\mu_0}{2} e^{-kz} \left(\frac{k_y}{k} j_x(k_x, k_y) - \frac{k_x}{k} j_y(k_x, k_y) \right). \tag{2.9}$$

In this research, B_z is the only measured component It does not determine both J_x and J_y According to current density obeys the equation of continuity, $\nabla \cdot J = 0$, the following equation is also obtained in the transform space.

$$-ik_x j_x(k_x, k_y) - ik_y j_y(k_x, k_y) = 0 \tag{2.10}$$

From Eq. (2.9) and (2.10), j_x and j_y can be solved as

$$j_x(k_x, k_y) = -\frac{2i}{\mu_o} \frac{e^{kz_0}}{k} k_y b_z(k_x, k_y, z), \tag{2.11}$$

and

$$j_y(k_x, k_y) = \frac{2i}{\mu_o} \frac{e^{kz_0}}{k} k_x b_z(k_x, k_y, z). \tag{2.12}$$

In Eq. (2.11) and (2.12), z_0 is lift-off distance that from superconductor layer to hall probe.

Because of the measurement noise as increase as signal is amplified, the harmonic component must be eliminated. In this research, we applied Hanning window,

$$w(k) = \begin{cases} \frac{1}{2}\left(1 + \cos\frac{k}{k_{cut-off}}\pi\right) & \text{for} \quad k \leq k_{cut-off} \\ 0 & \text{for} \quad k > k_{cut-off} \end{cases} \tag{2.13}$$

The cut-off frequency, $k_{cut\text{-}off}$ is the cut-off wave number. The spatial resolution is determined by $k_{cut\text{-}off}$, which is employed in this investigation. The sheet current density distribution J_x and J_y in Eq. (2.11) and (2.12) can be calculated after removing the noise component by multiplying this Hanning-filtered equation.

2.1.3 Estimation of longitudinal distribution of local critical current

The current I_c distribution in the longitudinal direction is obtained from the sheet current density distribution by integrating the absolute value of J_x across the width direction, a longitudinal 1D I_c distribution can be derived, as known in Fig. 2.6. If the cut-off wavelength $\lambda_{cut-off}(= 2\pi/k_{cut-off})$, is too large in relation to the width of the tape, information on the point where the current reciprocates in the middle of the tape width is missing. In Fig. 2.7, this relationship depends on the width, w and the $\lambda_{cut-off}$, and taking this into account, I_c can be obtained using the following equation.

$$I_c = \frac{w}{w - 0.6\lambda_{cut-off}} \int_{-\infty}^{\infty} |J_x| \, dy \tag{2.14}$$

In this study, the vector sum of the sheet current densities J_x and J_y was taken to evaluate the two-dimensional J_c distribution in the longitudinal direction, taking into account the current flowing in the width direction Using $J = \sqrt{J_x{}^2 + J_y{}^2}$, the one-dimensional I_c was derived by performing calculations using $|J_x|$ in Equations 2.14 as J.
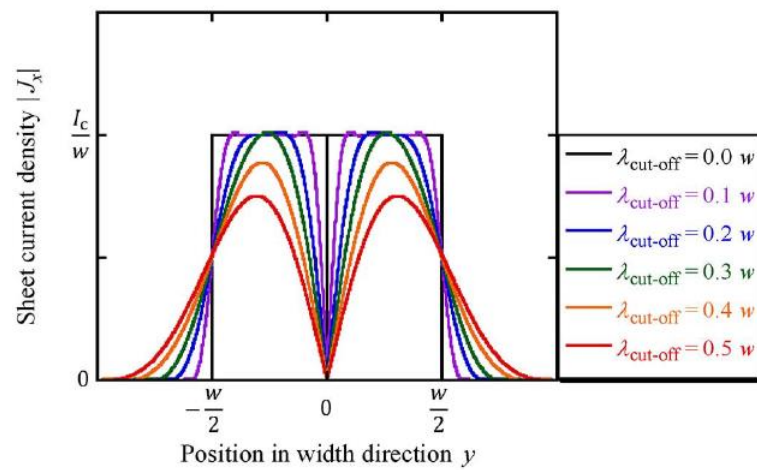
Fig. 2.6 the lateral $|J_x|$ distribution for different values of $\lambda_{cut-off}$ [31]
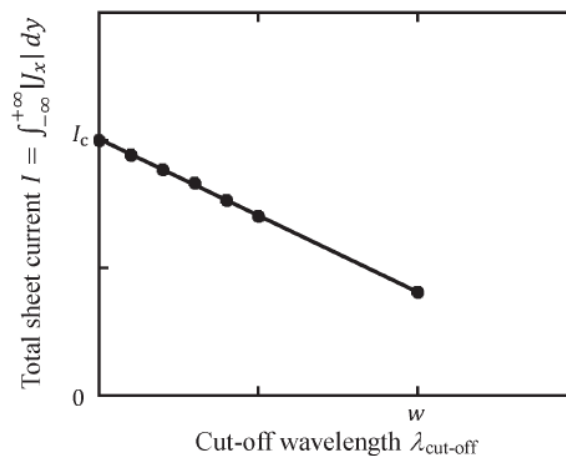
Fig. 2.7 Relationship between the total sheet current, I, (the area of the lateral distributions shown in Fig. 2.6) and their cut-off wavelength [31]

2.2 Tapestar[TM] system

2.2.1 Principle of Tapestar[TM] [29], [38]

Tapestar[TM] is a as a de facto standard characterization for determining local critical current by measuring the magnetization of superconducting tapes, as shown Fig. 2.8. The tape is constantly supplied by a feed reel and travel under liquid nitrogen and the perpendicular magnetic field applied by a coil while the tension and position of the tape are controlled. The measurement may be done at a maximum speed of 200 m/h, with a longitudinal resolution of around 1.1 mm. the schematic of the system is shown in Fig 2.9.

Fig. 2.8 The Tapestar[TM] system [38]
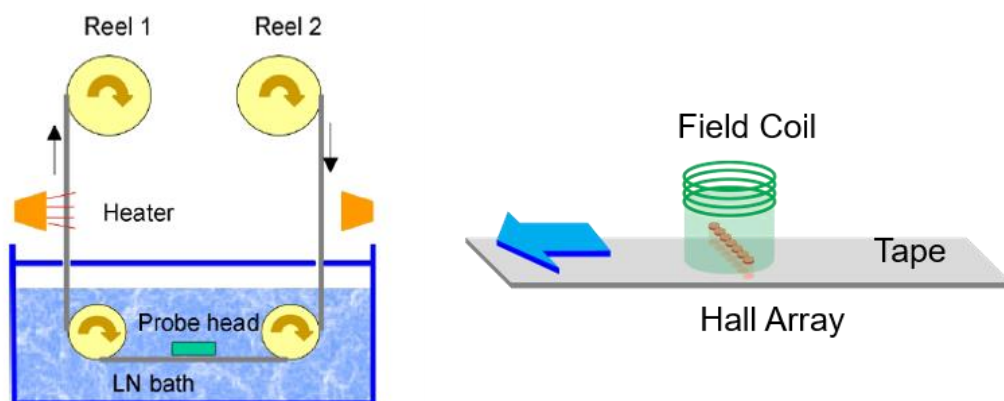
Fig. 2.9 The schematic of Tapestar[TM] system [29]

For estimation of longitudinal distribution of local critical current, the magnetic field penetration into the superconducing tape measured by an array of Hall sensor is shown by the blue points in Fig. 2.10. The distribution of the thin black line passing through the blue points is the magnetic field penetration when an external magnetic field is applied to the tape and the thick black line on the *x*-axis represents the tape area. The measure field penetration marked as the blue points. In general, there are 7 or 21 Hall arrays at equal intervals. It means that the higher resolution in the width direction can be achieved when number of array increase. As aresult, the magnetic field penetration is much more accurate.
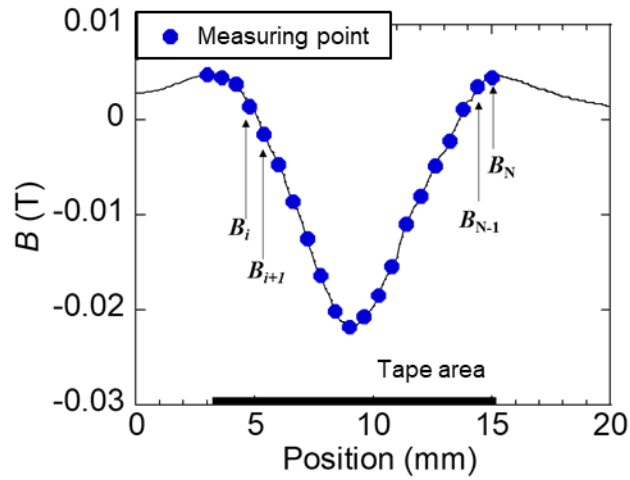
Fig. 2.10 Magnetic field penetration along width direction

The local critical current distribution is evaluated by continuously measuring this magnetic field distribution for the entire length. It is calculated by taking the root mean squares of the slope of the penetrating magnetic field across the width direction at each longitudinal position using an array of Hall elements. It is derived by the following equation (2.15).

$$I_{\mathrm{c}} = \alpha \sqrt{\sum_{i=1}^{N-1} \frac{(B_{i+1} - B_i)^2}{N-1}} \qquad (2.15)$$

α is a coefficient for calibration and is determined based on the actual values measured by the four-probe method. *N* means the number of Hall arrays in the measurement. As described above, Tapestar$^{\mathrm{TM}}$ provides the local critical current distribution in longitudinal position.

Chapter 3

Image classification for recognizing defect in HTS tapes

In this chapter, the basic principle of image analysis based deep leaning, the process of creating reliable image classification model for recognizing the local obstacles from microscopy images of HTS tape obtained by RTR-SHPM the evaluation and the matrices for image classification demonstrated the model performance were explained.

3.1 The basic principle of image classification based on the convolutional neural network [39-41]

Image classification is a deep learning (DL) that computer algorithm can learn from past data or experiences without being explicitly programmed. It is built based on convolutional neural networks (CNN) that extract underlying feature of input data, known as training data, in order not only to make reliable predictions or decisions but also to make more sense to humans. Image classification is used to classify an image into different classes or categories.

3.1.1 Neural networks

(1) Forward Propagation

The forward propagation is first step in the neural networks to extract the important information from input. The output is extracted from very layers and passed on to the next layer until its output is computed at last layer. They are comprised of node layers containing an input layer, one or more hidden layers, and an output layer. The block diagram of neuron networks consisting of these layers is shown in Fig. 3.1.
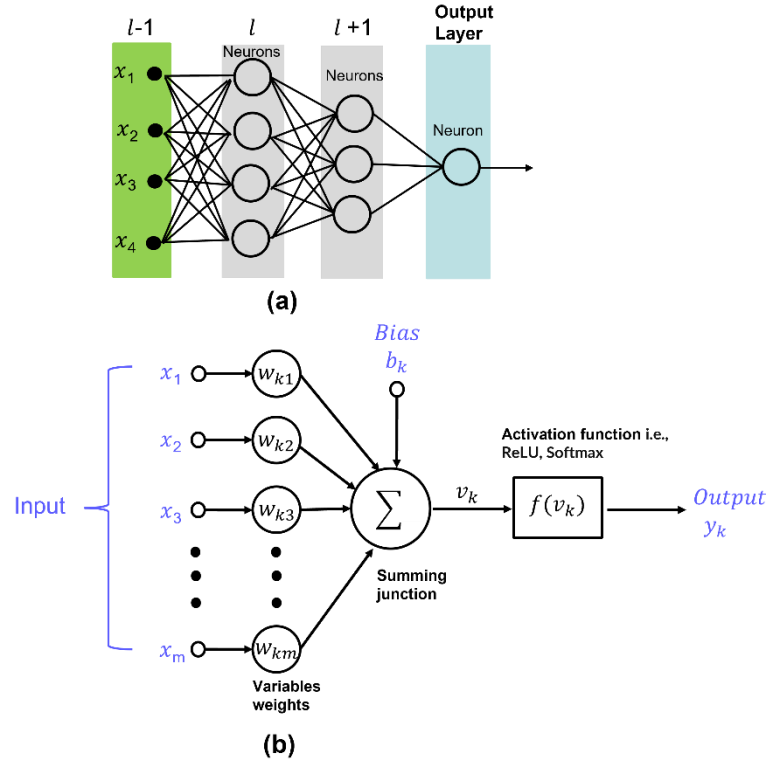
Fig. 3.1. The block diagram of neuron networks in mathematical terms (a) deep neuron networks and (b) single neuron [39]

In the case of fully connected artificial neural network, all inputs are multiplied by their respective weights and summed. Then, each node connects to another and has an associated bias, defined by

$$v_k = \sum_{j=1}^{m} w_{kj} x_j + b_k \tag{3.1}$$

where x_j is the jth input signals, w_{kj} is the weight for the connection to the kth neuron and b_k is the bias at the kth neuron. Then, the sum of input to the kth neuron, v_k. The output from the kth neuron denoted by y_k is obtained by passing through an activation function f as follows.

$$y_k = f(v_k) \tag{3.2}$$

Then, the y_k is connected to the next layer as an input signal.

We now consider the connection among the neurons in the lth and the $(l+1)^{\text{th}}$ layer. We will use w_{kj}^{l+1} to denote the weight for the connection from the jth neuron in the lth layer to the kth neuron in the $(l+1)^{\text{th}}$ layer. Similar notation is also used for the

biases and outputs, i.e., b_k^{l+1} is for the bias if the kth neuron in the $(l+1)^{th}$ layer, and y_k^l is the output from the kth neuron in the lth layer.

$$v_k^{l+1} = \sum_{j=1}^{m} w_{kj}^{l+1} y_j^l + b_k^{l+1} \tag{3.3}$$

$$y_k^l = f(v_k^l) = f\left(\sum_{j=1}^{m} w_{kj}^l y_j^{l-1} + b_k^l\right) \tag{3.4}$$

(2) Activation Function

The activation function is the function that decides whether a neuron should be activated or not. This means that if the input is more important to the network or higher than threshold value, the input should be taken into account by applying mathematical activation functions. Therefore, the activation function in a neural network is used to transfer the weighted sum of the input from the node into the output value to give neural nonlinear expression ability.

Generally, the non-linear activation function used in the neural networks or deep learning is the rectified linear unit (ReLU) function. It is a standard function for hidden layers in the deep neural networks.

$$f(v) = \max(0, v) \tag{3.5}$$

$$f(v) = \begin{cases} v & \text{if } v > 0 \\ 0 & \text{if } v \leq 0 \end{cases} \tag{3.6}$$

When the inputs are positive, this function returns the same value as the input, and when the inputs are negative or 0, it returns 0. The gradient is not continuous, but it is constant. The ReLU is described by the graph in Fig. 3.2.
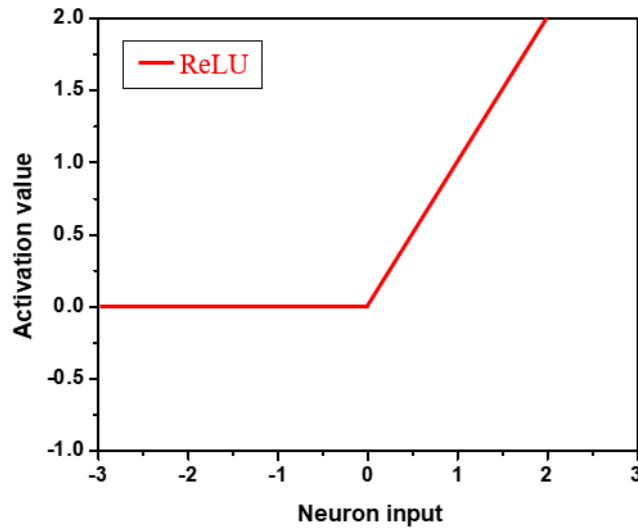
Fig. 3.2 The graph of rectified linear unit (ReLU) activation function.

(3) Classification and Its Confidence Value

In the very last layer *L*, the softmax activation function is used for classification. The softmax function takes a vector of real numbers as input and normalizes it into a probability distribution with probabilities proportional to the exponentials of the input numbers as shown in the following equation. It transforms the numerical value into a probability of a specific class between 0 and 1 by summing all classes.

$$\hat{y}_k = S(y_k^L) = \frac{e^{y_k^L}}{\Sigma_{j=1}^n e^{y_j^L}} \tag{3.7}$$

where, $\hat{y}_k$ is probability score for the class *k*.

n is the total number of classes.

y_k^L is output score for the class *k* in last layer *L*.

As can be seen, the softmax function is essentially same to the Boltzmann distribution which gives the probability distribution of states with its energy. From this analogy, it is reasonable that the softmax function gives us the confidence value of the predicted class in the classification.

(4) Loss Function

To evaluate the performance of a classification model, cross-entropy loss is generally used in the classification as described below. The loss value will decrease as the predicted probability close to the actual label results in a low loss value. It is defined as the following.

$$E = -\sum_{k=1}^{n} y_k \log \hat{y}_k \tag{3.8}$$

where, E is the loss value.

y_k is output score of the ground truth for the class k.

$\hat{y}_k$ is the predicted value for the class k.

In a binary classification task, where $n = 2$ (total number of classes) , the cross-entropy loss is defined as.

$$E = -y_1 \log \hat{y}_1 - (1 - y_1) \log(1 - \hat{y}_1) \tag{3.9}$$

(5) Backpropagation

During the training process of deep neuron network, the first step follows forward propagation in the network, where the data is passed through all layers, from the input layer to the output layer. After that, the loss function is calculated at final output layer by comparing between predicted value and ground truth value. In order to minimize this loss value calculated by the forward propagation, the backpropagation is used to calculate the gradient descent for minimizing the loss function by adjusting weights and biases.

We start consideration from the influence of total input v_k^L to the kth node to the output error at the very last layer L. We define the error δ_k^L as follows.

$$\delta_k^L \equiv \frac{\partial E}{\partial v_k^L} \tag{3.10}$$

Using chain rule, we can obtain following relationship.

$$\delta_k^L \equiv \frac{\partial E}{\partial v_k^L} = \sum_j \frac{\partial E}{\partial y_j^L} \frac{\partial y_j^L}{\partial v_k^L} = \frac{\partial E}{\partial y_k^L} \frac{\partial y_k^L}{\partial v_k^L} = \frac{\partial E}{\partial y_k^L} f'(v_k^L) \tag{3.11}$$

Note that

$$\frac{\partial y_j^L}{\partial v_k^L} = \begin{cases} 0 & \text{for } j \neq k \\ f'\left(v_k^L\right) & \text{for } j = k \end{cases} \tag{3.12}$$

We can then extend it to the error of neuron k in the lth layer, denoted by δ_k^l.

$$\delta_k^l \equiv \frac{\partial E}{\partial v_k^l} \tag{3.13}$$

By using chain rule technique,

$$\delta_k^l \equiv \frac{\partial E}{\partial v_k^l} = \sum_j \frac{\partial E}{\partial v_j^{l+1}} \frac{\partial v_j^{l+1}}{\partial y_k^l} \frac{\partial y_k^l}{\partial v_k^l} = \sum_j \delta_j^{l+1} \frac{\partial v_j^{l+1}}{\partial y_k^l} \frac{\partial y_k^l}{\partial v_k^l} \tag{3.14}$$

From Eqs. (3.3), and (3.4)

$$\frac{\partial v_j^{l+1}}{\partial y_k^l} = w_{jk}^{l+1} \tag{3.15}$$

Therefore,

$$\delta_k^l = \sum_j \delta_j^{l+1} w_{jk}^{l+1} f'\left(v_k^l\right) \tag{3.16}$$

We can think of this as moving the error backward through the network from the very end layer L, then can obtain the error at arbitrary layer l. Next, we consider the influence of weights and biases by the partial derivative of loss function by weights and losses. Using the chain rule, the derivatives for weight at the lth layer can be obtained as follows.

$$\frac{\partial E}{\partial w_{kj}^l} = \frac{\partial E}{\partial v_k^l} \frac{\partial v_k^l}{\partial w_{kj}^l} = \frac{\partial E}{\partial v_k^l} \frac{\partial \left(\sum_{j=1}^m w_{kj}^l y_j^{l-1} + b_j^l\right)}{\partial w_{kj}^l} = \delta_k^l y_j^{l-1} \tag{3.17}$$

Similar way, the derivatives for the biases in the lth layer can be obtained as follows.

$$\frac{\partial E}{\partial b_k^l} = \frac{\partial E}{\partial v_k^l} \frac{\partial v_k^l}{\partial b_k^l} = \frac{\partial E}{\partial v_k^l} \frac{\partial \left(\sum_{j=1}^m w_{kj}^l y_j^{l-1} + b_k^l\right)}{\partial b_k} = \delta_k^l \tag{3.18}$$

We can calculate those derivatives by δ_j^l using backpropagation. This then allows us to adjust (train) the weights and biases to minimize the loss function. To decrease the error, we then subtract this derivative value from current value multiplied by a learning rate γ as follows.

$$w_{kj}^{'}{}^{l} = w_{kj}^{l} - \gamma \delta_k^l y_j^{l-1} \qquad (3.19)$$

$$b_k^{'}{}^{l} = b_k^{l} - \gamma \delta_k^l \qquad (3.20)$$

where, γ is learning rate.

w_{kj}^l is the old weight in the lth layer.

$w_{kj}^{'}{}^{l}$ is the new weight in the lth layer.

b_k^l is the old bias in the lth layer.

$b_k^{'}{}^{l}$ is the new bias in the lth layer.

3.1.2 Convolutional neural networks (CNNs)

In the fully connected neural network, the numbers of parameters become so large for the analysis of images. To reduce the parameters by keeping the local relationship, convolutional neural networks (CNNs) are now widely used for DL based image analyses such as classification and object detection. They have a large amount of data and can be computationally demanding, requiring graphical processing units (GPUs) to train models. They consist of three main layers: convolutional, pooling, and fully connected. In principle, convolutional neural networks, do not link every neuron in each layer to every neuron in the next layer, relying on weight sharing instead. The weights are connected locally, meaning one node only links to nodes in the following layer. This concept is beneficial for images because it is reasonable to assume that every pixel has some correlation to the neighbors.

(1) Convolutional Layer

An image is represented as matrices in the computer by their RBG values. This means that image input will have three dimensions, height, width, and depth, corresponding to RGB in an image. Therefore, the convolution process starts with extracting the features from the pixel using a kernel or a filter, which will move over the image fields, checking if the feature is present. The kernel is a two-dimensional (2-D) array of weights representing part of the image. The filter is then applied to a part of the image, and the dot product between the input pixels and the filter is calculated, so the filter then shifts by a stride and repeats the operation until the kernel has swept

across the entire image. This dot product is then supplied into an array of outputs. The illustration of convolutional layer is shown in Fig. 3.3. The final feature map is the ultimate output of a series of dot products from the input and the filter.
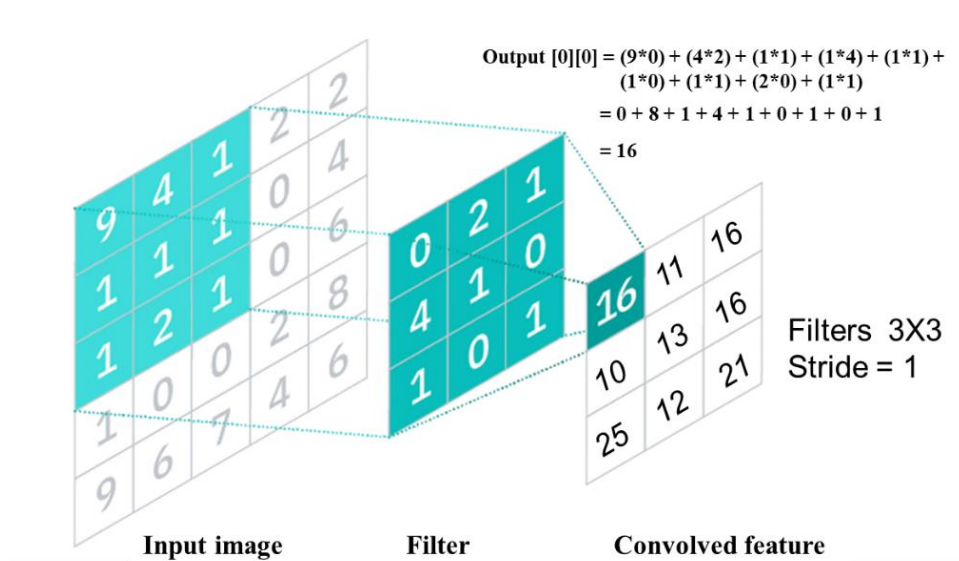

Fig. 3.3 Convoluted feature output [42]

(2) Pooling Layer

Pooling layer, also known as down sampling, reduces the number of parameters in the input by performing dimensionality reduction. The pooling process, like the convolutional layer, sweeps a filter across the whole input, but this filter does not contain any weights. Instead, the kernel applies an aggregation function on the receptive field values, creating the output array. There are two main types of pooling. Firstly, max pooling is the filter that take the pixel with the highest value to the output array as the filter moves across the input. Secondly, Average pooling is the filter, which calculates the average value within the receptive field and sends it to the output array. In comparison to average pooling, this strategy is employed more frequently.

The illustration of 2x2 pooling applied to 3x3 convoluted feature is shown in Fig. 3.4. While the pooling layer loses a lot of information, it does provide certain advantages for the CNN. They assist in reducing complexity, increasing efficiency, and reducing the danger of overfitting.
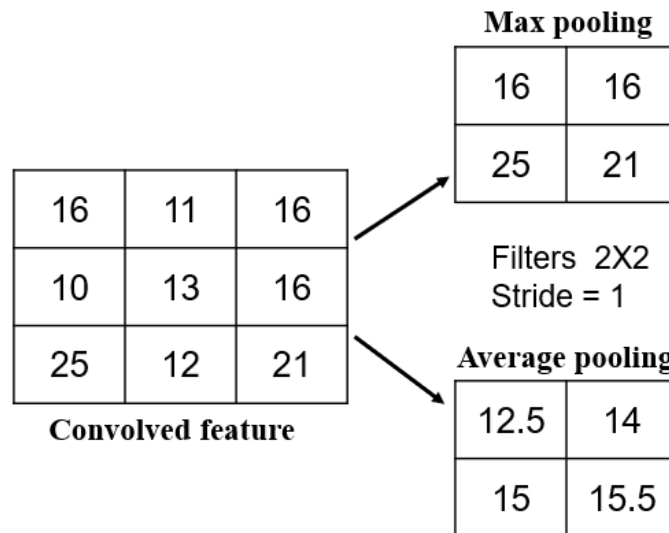
Fig. 3.4 The illustration of two pooling types with 2x2 filters and stride 1

(3) Fully Connected Layer

After passing through the final convolution and pooling layer, the data is flattened or transformed into a one-dimensional (1D) array of numbers (or vector) and then fed into the fully connected layer, which has full connections to every neuron in another layer, as seen in regular artificial neural networks. The flattened array goes through the fully connected layer to classify the images by using activation function such as softmax.

(4) GoogLeNet Architecture

One of the difficulties in this study is the limited number of training data sets especially for defect regions. We first identified local defects by use of local critical current criterion, however, the numbers of the defects are still relatively small because the samples investigated in this study are practical industrial materials. In order to develop reliable image classification model from such limited number of data sets, we adopted a pre-trained well-known GoogleNet architecture, and fine-tune its parameters through training using our own images.

The GoogleNet was pretrained on approximately 1.28 million images (1,000 object categories) from ImageNet dataset with an error rate of 6.67%. The architecture consists of 22 layers deep, with 27 pooling layers included and 9 inception modules

stacked linearly in total, as known in Fig. 3.5. All inception models compute the feature at different scales using variable size convolutional filters, namely 1×1, 3×3 and 5×5 and an additional 3×3 max pooling to capture more discriminative features from the pattern passed from the previous layer. These four branches all use same padding to give the input and output the same height and width before concatenating into a single output vector forming the input of the next stage. After that, the output is passed on to the classifier, which composes of one average pooling layer, one convolutional layer, two fully connected layers with 1,000 units, and a softmax activation layer for estimating class probabilities. We reduced the output of the fully connected layers from 1000 categories to 2 for our purpose to produce a binary output. All convolutional layers in this network use the ReLU activation function. Moreover, during the training process, two more auxiliary classifiers are plugged on top of the third and sixth inception modules to calculate the overall loss.

This approach allows us to develop a reasonably high performance image classification model even from small number of defect images. Detailed results are described in section 3.2.
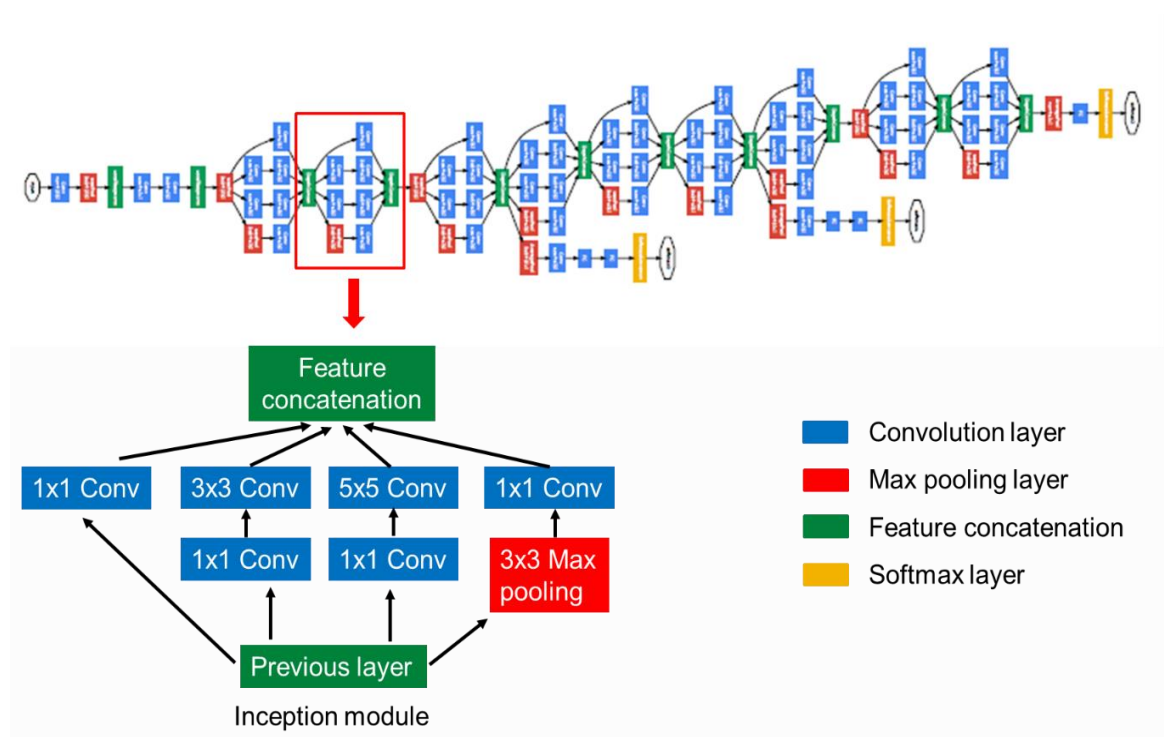
Fig. 3.5 GoogLe5Net architecture based on CNN [41]

3.1.3 Deep learning platform provided by IBM PowerAI vision

Deep learning is basically a type of machine learning and made up of very deep with multiple hidden layers based on complicated convolution neuron network. It has been popular utilized to help the computer perform the difficult tasks through perception, more like the way human does. However, according to the complicated algorithms behind the deep learning, IBM PowerAI Vision has now provided a complete platform for image analytics, such classification and object detection by wrapping up the complex code tasks for users. It invents the model on top of based deep learning so that we can get the most accuracy model. Hence, we can create, label, train, validate, and deploy the models easily for image analytics. The simple outline of IBM PowerAI Vision is shown in Fig. 3.6.

Fig. 3.6 The outline of IBM PowerAI Vision [43], [44]

3.2 Building image classification model

3.2.1 Data preparation

(1) Sample

The commercials long REBCO coated conductors manufactured by the different manufacturers, and each specific tape is shown in Table 4.1.

Table 3.1 The specification of the investigated commercial long tape

Manufacturer		Fujikura
Specification	Fabrication process	IBAD/PLD
	Width [mm]	4
	Length [m]	200
	Total thickness [mm]	0.16
	Rare earth	Gd
	Substrate	Hastelloy C-276
	Substrate thickness [μm]	75
Performance @77K, SF	I_c [A] guaranteed	>250

(2) Data Set

The data set is 2D critical current density mapping images taken from the RTR-SHPM. The distribution of critical current density, J_c flowing along the CCs gives information about 2D inhomogeneity as well as I_c obtained by integrating the corresponding J_c across the width of tape. These images were collected every 50 mm in length and with 10 mm in width. The entire data set consisted of 4047 images along the CC. The example of 2D J_c mapping images, including minimum critical current, $I_{c,min}$ value in each image is shown in Fig. 3.7.
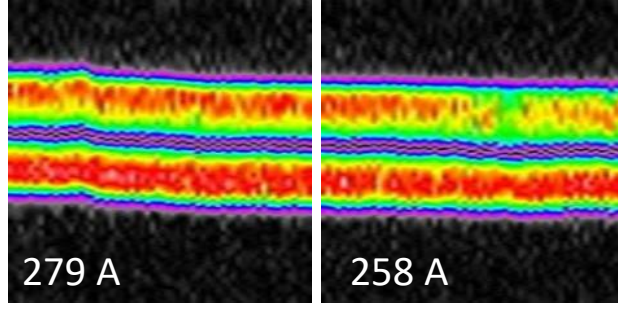
Fig. 3.7 The example of 2D J_c mapping images

3.2.2 Training set

The training set is a set of data used to teach the model to learn the hidden features in the data. We used J_c images containing local obstacles for this training data set. According to the localized drop in the magnetization current visualized by the RTR-SHPM technique, we defined the position at where the magnetization current drop locally as a position of defect related to the large discrete local I_c drops [27], [45]. The local I_c drops used as minimum I_c value ($I_{c,min}$) of each image was also collected and assumed to be relevant to the defect/normal position within the image. The statistical probability distribution of the $I_{c,min}$ value for all images is displayed in the histogram with a semi-logarithmic plot in Fig. 3.8. By studying the statistical distribution, we can identify the group of $I_{c,min}$ distribution by double peak separated by the $I_{c,min}$ at around 245 A. This distribution indicated the group in the $I_{c,min}$ lower than 245 was dominated by extrinsic defects, not by an intrinsic I_c distribution. We selected these 8 images from this region for the training category. However, the model needs to separate these defects by knowing the different matrix between defect and normal region. The clear normal region image is very important for training the normal region. These normal images were selected from the normal position with higher than an average $I_{c,min}$ of 275 A. There were 100 images available for the normal category. Finally, the model technically learns the underlying features from these two training categories. The example of J_c images of two categories, including local $I_{c,min}$ value in each image is shown in Fig. 3.9.
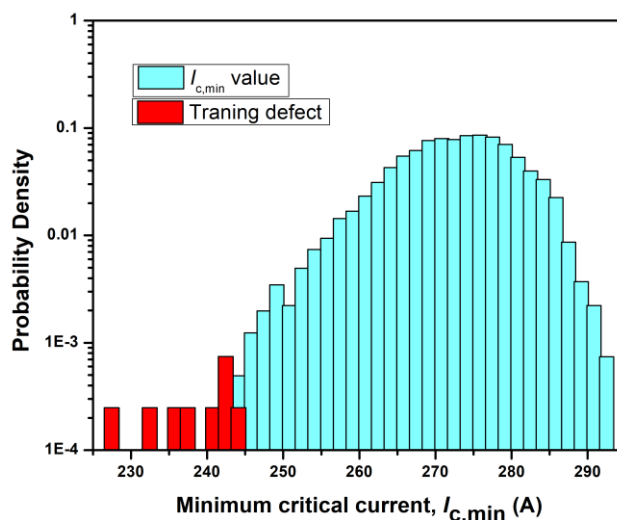
Fig. 3.8. The histograms of all $I_{c,min}$ values for all images along the CC, including training defect group at around lower $I_{c,min}$ of 245 A
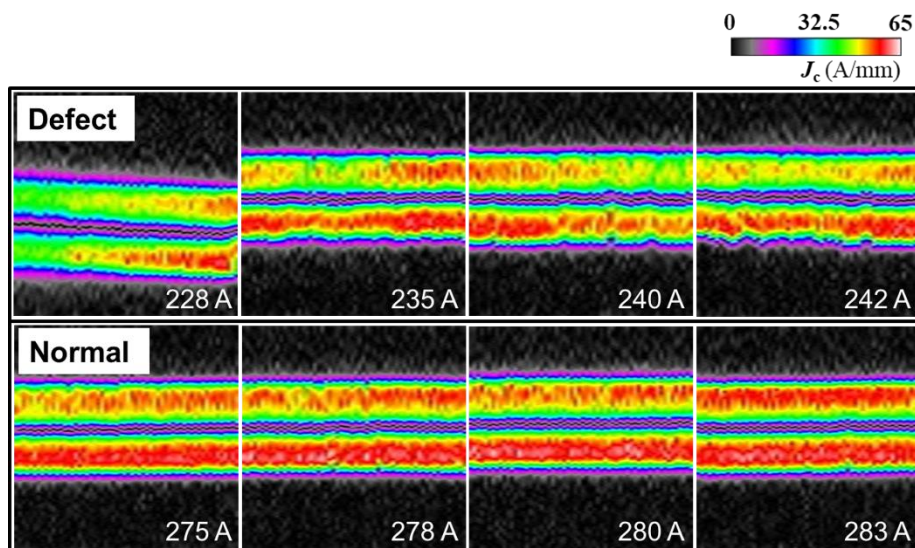

Fig. 3.9. The example of J_c images of two categories, including $I_{c,min}$ values

3.2.3 Performance of the image classification model

In this research, we used the GoogLeNet architecture [41], a Deep Convolutional Neural Network (DCNN) developed by researchers at Google via the IBM PowerAI Vision platform. The platform offers built-in deep learning models that learn to analyze images for classification. It wraps up the complex code tasks in a simple to learn and use web interface.

We trained the model using Graphics Processing Units (GPU). The labeled training data sets were automatically divided into two for training and validation with the ratio of 0.8, i.e., 80% of the images in the data set (at random) being used for training and 20% being used for validation [44]. All model hyperparameters as illustrated in Table. 3.2.

Table 3.2 The Model hyperparameters of model.

Model hyperparameter	value
Learning rate	0.001
Weight decay	0.0005
Test interation	100
Max interation	1500
Test interval	10
Ratio	0.8

The data was passed through the training algorithm with 700 iterations and a learning rate of 0.001 and weight decay to minimize the loss function and reduce the error during the training.

The relative performance of the image classification model can be shown by increasing to high accuracy of 100% whereas the training loss and test loss both decreased close to zero with similar tendency during the iteration process, as shown in Fig. 3.10. This model could be shown a good fit for the learning algorithm with high reliability at the end of the training process without over fitting.
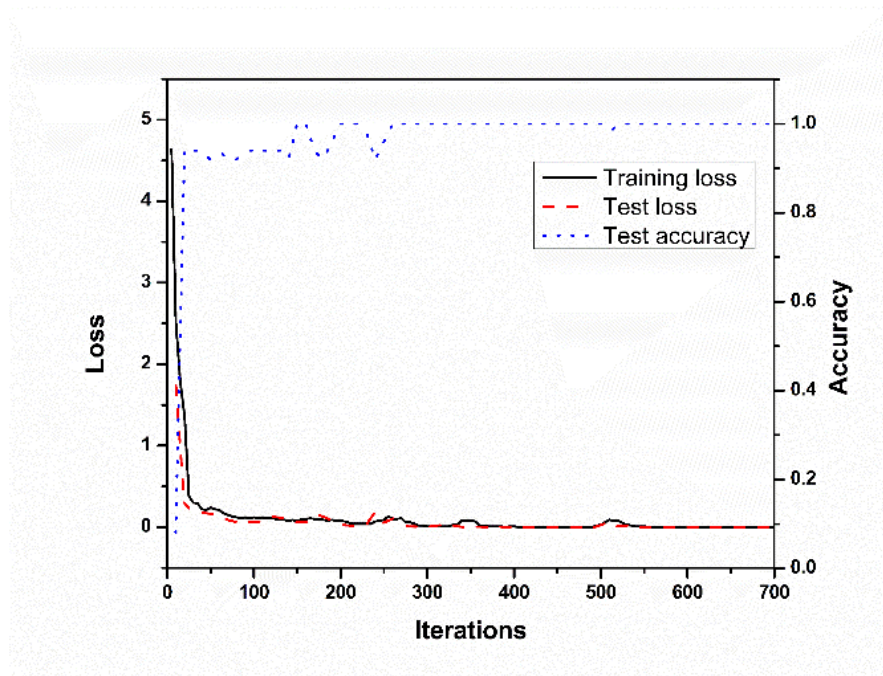
Fig. 3.10. Graph of loss and accuracy vs iterations during the training process of the image classification model

3.3 Evaluation of the image classification model [46]

The evaluation is an essential part of machine learning to determine the performance of the models. The confusion matrix is commonly used to evaluate the performance of the classification task. It displays a table for visualizing more detailed predictions of correct and incorrect classifications for each class. This matrix consists of 4 different combinations of predicted and actual values, as shown in Fig 3.11.

Fig. 3.11 Confusion matrix

Note that a binary classification problem has only two classes to classify, preferably a positive and a negative class. The definition of the abbreviations in each cell is described below.

Where, True Positive (TP): It means that the number of predictions has correctly predicted the positive class as positive.

True Negative (TN): The number of predictions has correctly predicted the negative class as negative.

False Positive (FP): The number of predictions has incorrectly predicted the negative class as positive.

False Negative (FN): The number of predictions has incorrectly predicted the positive class as negative.

By taking advantage of this confusion matrix, we can measure the other metrics such as recall, precision and accuracy. Recall is a measure of how accurately our model can identify the relevant data and sensitivity of the model. It is defined as the proportion of correct classifications to actual images in that class, as the following equation (3.21).

$$Recall = \frac{TP}{TP+FN} \tag{3.21}$$

Precision is the quality of repeated predictions made by the model. It is defined as the proportion of correct classifications to total predictions, as the following equation (3.22).

$$Precision = \frac{TP}{TP+FP} \tag{3.22}$$

Whenever data for test is an imbalance, using recall or precision alone cannot evaluate the model performance well. As shown in equation (3.23), the F1-score is a matric that balances the precision and recall in a single measure by considering the weighted harmonic mean.

$$F1 = \frac{2*Precision*Recall}{Precision+Recall} \tag{3.23}$$

The overall accuracy of the model, meaning the ratio of the total samples that were correctly classified, compared to the total samples. It can calculate by using the following equation (3.24) below.

$$Accuracy = \frac{TP+TN}{TP+TN+FP+FN} \qquad (3.24)$$

We set up images used for this confusion matrix evaluation using 200 J_c map images at various $I_{c,min}$ values selected from the whole 4047 images along the CC. For actual classes, 90 images are defect class as 110 images are normal class. The image classification model can perform well with these images that 22 actual defect images were misclassified as normal class, as shown in Fig. 3.12. From this confusion matrix, we can also calculate metrics such as accuracy, precision, and recall. The score of the image classification model is as follows: accuracy of 93.7%, precision of 100%, and recall of 75.6%.

Fig. 3.12. Confusion matrix for image classification model

3.4 Image classification result of a 200 m long commercial REBCO tape used for creating model

3.4.1 Classification result

The image classification could classify any local defects based on the shape of 2D J_c mapping related to the size and position of defects at a different local $I_{c,min}$ value as shown in Fig. 3.13. The reliability of the decision was also shown by a heat map and the highest confidence relating probability of classification.

The heat map obtained from gradient-weighted class activation mapping (Grad-CAM) [47] can help to understand which regions of an image led a CNN to its final classification decision by producing the heat map of class activation over input images. In order to obtain this class discriminative localization map Grad-CAM of width (u) and height (v) for any class c, (i.e., 2D for normal and defect map) so, it first computes the gradient of the score for class c, y^c (before the softmax), with respect to feature maps with the width (from i to u) and height (from j to v) dimensions, A_{ij}^k of the convolutional layer. And then, these gradients are applied to global average pooling (GAP) over 2D dimensions to obtain the neuron importance weights α_k^c.

$$\alpha_k^c = \frac{1}{Z}\sum_{i=1}^{u}\sum_{j=1}^{v}\frac{\partial y^c}{\partial A_{ij}^k} \tag{3.25}$$

Where, $\frac{1}{Z}\sum_{i=1}^{u}\sum_{j=1}^{v}$ is the global average pooling in the width and height dimensions

Z is the total number of elements in feature map, $Z=uv$.

K is the number of feature maps *(i.e., K=3; A^1* (red), A^2 (green), and A^3 (blue))

This α_k^c is a partial linearization of the deep network downstream from A^k that captures the importance of the feature map for a target class c. To obtain Grad-CAM, the weighted combination of forward activation maps follows by a ReLU.

$$L_{Grad-CAM}^c = ReLU(\sum_k \alpha_k^c A^k) \tag{3.26}$$

Where, α_k^c is neuron importance weight.

$L_{Grad-CAM}^c$ is Grad-CAM heatmap.

$ReLU$ is the activation function.

The idea behind Grad-CAM is to take advantage of a specific kind of convolutional neural network architecture to produce heat map visualizations. It could help us determine whether the model has correctly learned the features of this classification. The red area of the heat map in the defect images corresponds to the areas that were of the highest relevance with the defect position.
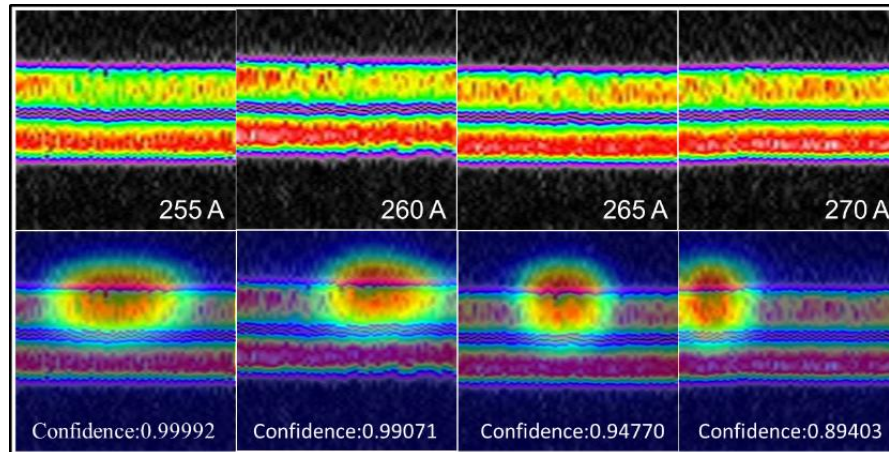
Fig. 3.13 The example of J_c mapping images at different $I_{c,min}$ containing defect classified by image classification, along with heat map images and score of confidence in lower images

Furthermore, the 2D J_c mapping images containing defect and normal images with the same I_c drop value were still classified and compared to the I_c variation around the area measured, as shown in Fig. 3.14. The defect images at I_c drop of 270 A corresponded to the deduction of the intensity of J_c mapping at the curtain defect position. The local I_c drop around the defect tended to broaden along the longitudinal direction, which referred to the defect size whereas the normal area could also be classified without any significant large obstacle related to intrinsic I_c fluctuation and provided the heat map responded to the whole region on the tape in the images.
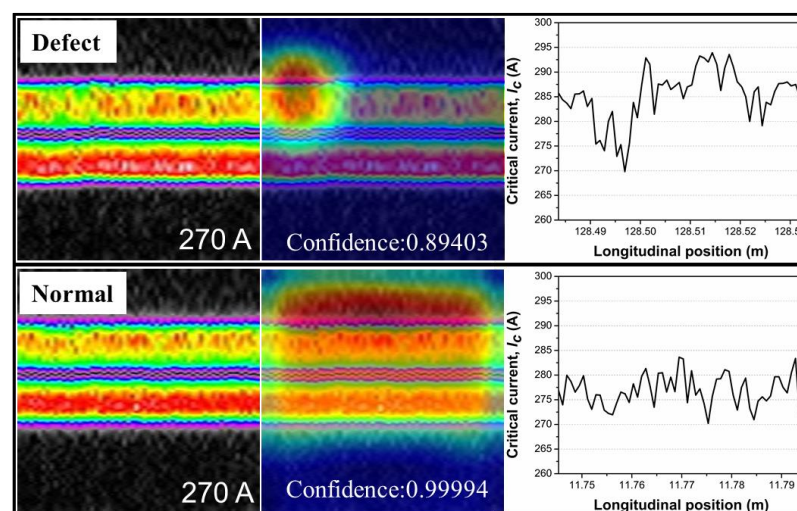

Fig 3.14 Comparison between a defect and normal image at the same local $I_{c,min}$ of 270 A, including I_c variation of both images

3.4.2 Statistic $I_{c,min}$ value classified by image classification

The long CC was recognized as defects by the image classification model. Most J_c mapping images were used to classify two different kinds of images as the training set. The classification model classified 372 images into defect category, including training defect images, and 3675 images into normal category, so the 9.2% out of All images divided 5 cm-length individually was the defect region. It indicates that the frequency of the local defect located at least 1-2 defects per 1m-length. Moreover, the distribution of defect images can be seen in the semi-logarithmic plot with the count of local $I_{c,min}$ distribution in Fig. 3.15. The histogram shows the relationship between the number of defect images and various local $I_{c,min}$ values. It displayed the distribution of defects with a wide I_c distribution value 228 A to 275 A. It indicates that many hidden localized defects at I_c drops at high values were still the existence and detected by image classification.
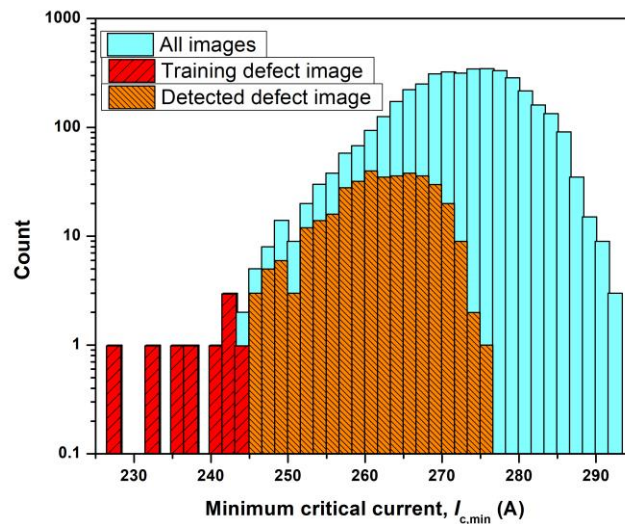
Fig. 3.15 Histogram with the probability density of local $I_{c,min}$ distribution of all images after being classified

3.4.3 Distribution of confidence value in the classification

In general, classifications can generally classify and provide confidence value showing the reliability of each prediction. The confidence value is a decimal number between 0 and 1, interpreted as a percentage of probability at last layer of CNN. Moreover, there is not any specific threshold for each class. It may be different from one class to another class. Therefore, the determination of the confidence value seems to be important to show the reliability of the classification.

After the whole images along the long length of the CC were passed to recognized defects by this model, Most J_c mapping images were used for classifying into two different kinds of images as the training set. The classification model classified 372 images into defect category, including the number of training defect images. The count of defect images with various confidence scores between 0.5 and 1 can be seen in the semi-logarithmic scale with the histogram as a function of local $I_{c,min}$ values in Fig. 3.16(a). It indicated that around 80 % of these defect images were classified well with a confidence score of more than 0.9, and the tendency of confidence value of these defect images seemed to decrease, as the $I_{c,min}$ value started to increase from 260 A, as shown in Fig 3.16(b). Because classification prediction is starting to be a hard task to discriminate defects from normal images based on training experience.

On the other hand, classification classified 3675 images into the normal image category with high confidence value, which 98% of normal images were higher than 0.9 of confidence score, as shown in 3.16(c). However, similar to the case of defect category, a low confidence value can be seen in the range of $I_{c,min} = 250{\sim}275$ A, which is close to the lower limit of $I_{c,min}$ in the category of normal, as shown in Fig. 3.16(d). The averaged confidence value in both categories as a function of $I_{c,min}$ was displayed in Fig. 3.16(e). It indicated that the confidence value increases as the $I_{c,min}$ decreases in the defect category, whereas the normal category has a high confidence value as the $I_{c,min}$ increases, and the crossover point is around $I_{c,min}$=260 A. It is very reasonable because local obstacles will suppress the $I_{c,min}$.
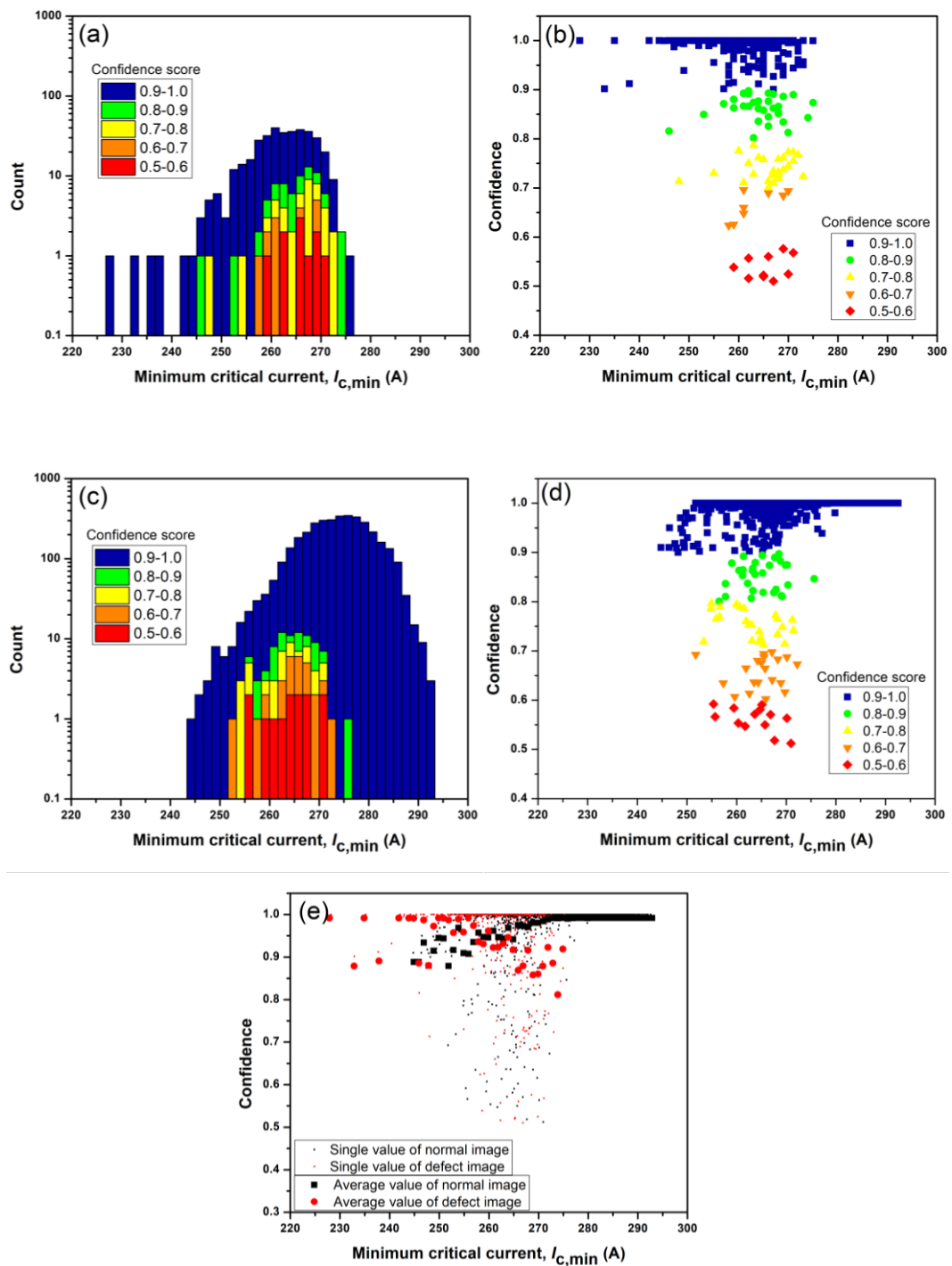
Fig. 3.16 Confidence values obtained by image classification: (a) histogram as function of local $I_{c,min}$ values with the number of defect images in semi-logarithmic scale (b) confidence of defect images vs local $I_{c,min}$ values (c) Histogram as function of local $I_{c,min}$ values with the number of normal images in semi-logarithmic scale. (d) confidence of normal images vs local $I_{c,min}$ values (e) confidence of both categories vs local $I_{c,min}$ values including an average of confidence overlayed.

3.4.4 Influence of imbalanced data

Imbalanced data is a crucial problem in the present analyses because the number of data set for defects are much less than that of normal region. In our case, it refers to learning patterns from the imbalanced data as an input for the training classification model using 8 and 100 images for defect and normal categories. These number of defected images were very much limited especially in the beginning of this research. We first identified the extrinsic defect based on a low local I_c criterion ($< 245A$).

To train a model with such limited train dataset, we adopted high performance pre-trained GoogleNet model as the basic architecture [48], [49] in our network. The GoogleNet was trained on the ImageNet database of images. We reduced the output of the fully connected layers from 1000 categories to 2 for our purpose to produce a binary output. We then fine-tune the parameters through the training using our own dataset. As a result, the classification can still perform to classify into both categories well after training with these imbalanced data. Moreover, the classification results can be seen from the reasonable heat maps that illustrate where the defect regions are located and the tendency of the confidence score.

However, based on the results of confusion matric, some categories of the J_c images with small size of defects (i.e., close to normal class) are still misclassified into normal due to the low number of training data for defect category that refer to imbalanced data resulting in more sensitivity to the majority class as normal category. For example, in some cases of less confidence value than 0.9, the images will contain a small defect that the model could not classify as a defect image, as shown Fig. 3.17, but the model responded to the possible position of the defect by the deficiency of heat map indicating the reliability and possibility of the more accurate model itself, including a good agreement with low loss value showing learning correctly. This result suggests that the imbalanced training dataset influences the threshold value in the classification.

Based on the classification obtained in the first model described in this chapter, we could further identify the defect images which were difficult in the initial stage, the model can carry out additional training by adding more defect images in the training. The result showed that much more images were classified as defect category and the

initial defects from original model were still classified by improved model. These results were displayed in the next chapter including the influence on the confidence value in the classification.

The influence of the imbalanced dataset on the precision of the classification is not yet fully understood in this analysis and the method to increase the training datasets for defect images need to be studied further as a future task.
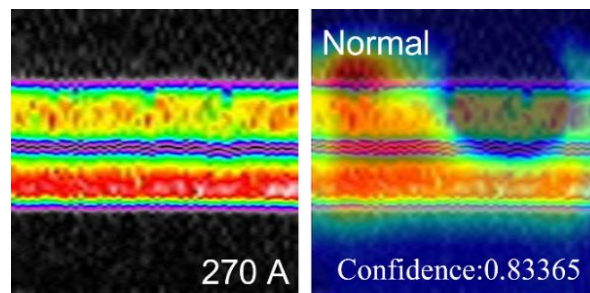

Fig. 3.17 The defect image was used as input data (left), and J_c image with the resultant heat map overlayed was classified as normal image, including confidence score (right).

Chapter 4

Further upgrade of the performance of the image classification

In this chapter, the improvement of defect recognition reliability was demonstrated after increasing the training data and using the training data with multi-categories. Then, the image classification was applied to different long HTS tapes to extract valuable information regarding the local obstacles so that the properties can be estimated based on this approach, which could not be identified by the conventional method.

4.1 Improvement of the reliability of the classification after additional training

For further improvement of the first classification model, the additional training images need to strengthen the network for higher performance of the classifier. Even though the first model succeeded in identifying the significant large obstacles in the J_c images well, the number of defect images, for example normal image with lower confidence than 0.9, was not still able to classify to defect categories. Based on this information, we considered training the model using the additional training defect images showing obstacles clearly and then took 33 normal images with the low confidence ranging from 0.5 to 0.7, as shown in Fig. 4.1. The example of the additional defect image, including the first model's result, is shown in Fig. 4.2.
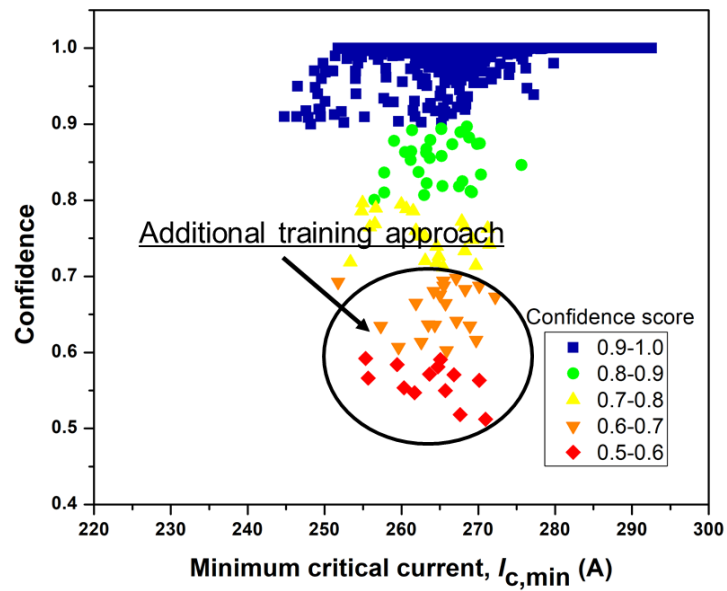
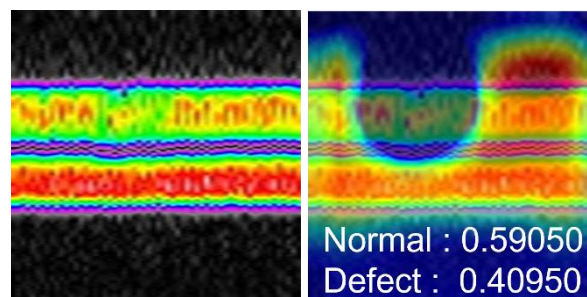Fig 4.1 Additional training defect image at low confidence of normal images

Fig 4.2 the example of additional training a defect image, including the result from the first model

After the model was retained on the traditional data combining the additional data, The performance of the improved model named model 2 is present by the loss value vs Iteration in Fig. 4.3. It indicated that the accuracy of model 2 was increasing over time during the training process while the loss of train and test value was going down to zero at the same time. At the end of the training process, model 2 was generated under reasonable learning curves without overfitting the data.

The confusion matrix used in the evaluation of model 2 is shown in Fig. 4.4. Four metrics were obtained from the binary confusion matrix, namely recall, precision,

accuracy, and F1-score, as illustrated in Table 4.1. As a result, all matrices of model 2 achieved a reasonably high value compared with model 1.
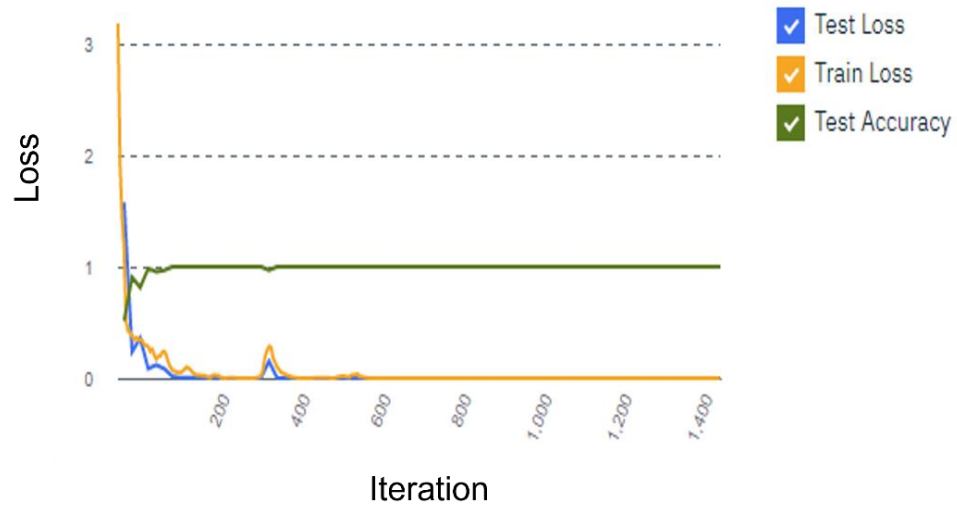

Fig. 4.3 Graph of loss and accuracy vs. iterations during training process of Model 2

Fig. 4.4 Confusion matrix of Model 2

Table 4.1 Metrics for evaluation of the classification models

Model	Recall	Precision	Accuracy	F1
1	0.756	1	0.937	0.861
2	0.967	0.936	0.955	0.951

Moreover, model 2 was able to classify 929 and 3118 images into the defect and normal categories. The number of defect and normal images vs the local $I_{c,min}$ value is shown in Fig. 4.5. The number of defect images is almost 2.5 times more than in model 1. It displayed the distribution of defects showing much more defects at $I_{c,min}$ value ranging 260-270 A and indicates that smaller obstacles at I_c drops at high values were still the existence and detected by model 2. The typical defect image that can be detected by model 2 compared to model 1, as shown in Fig. 4.6. The result shows that model 2 gave reasonable results with high confidence and heat map responding to the defect region in the J_c image. It means that the increase in the number of training data with critical defect images could improve much more performance of correctness.
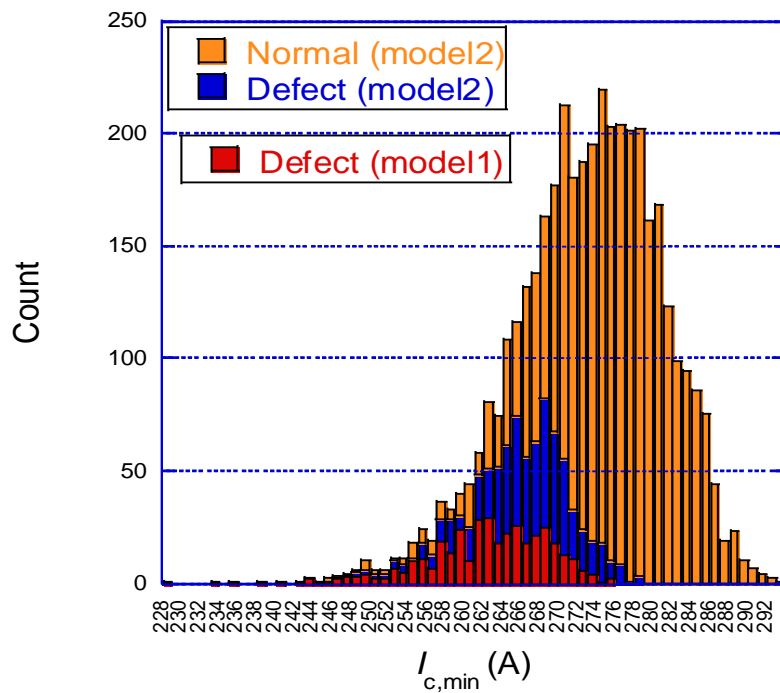

Fig. 4.5 The local $I_{c,min}$ distribution of all images after being classified into defect and normal by model 2 compared to model 1
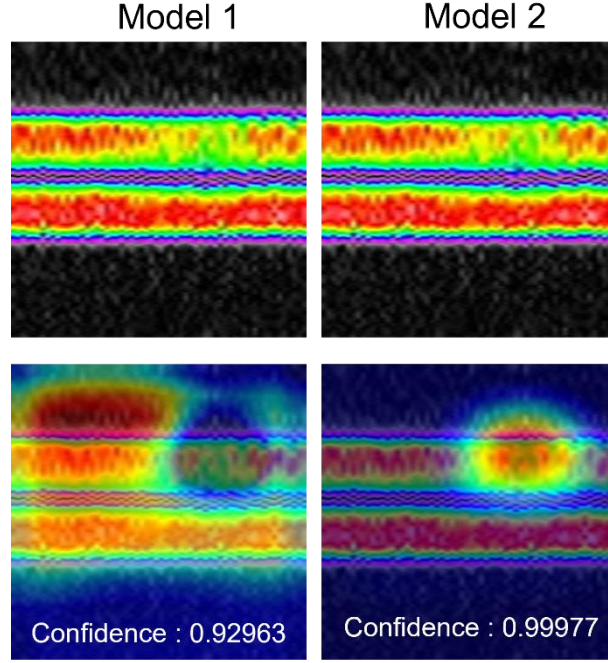
Fig. 4.6 Example of typical defect J_c images being classified by Model 1 and Model 2, showing heat map and confidence lower image

4.2 Image classification with multiple defect size categories

4.2.1 Data preparation for training set

Based on previous results of the classification model, it can only perform between defect and normal region based J_c image, but the sizes of obstacles were not classified. According to a localized drop in the magnetization current indicates the existence of the microstructural defects, it is possible to detect different defect regions as size by this image classification approach.

The different defect sizes need to be identified for use in the different training categories. However, the high resolution of the original J_c image consisting of the noise that came from a high special frequency component, we applied a Gaussian filter [50], which makes the 2D local average value in real space, to suppress the noise in the image resulting in the smoothed image. The following equation defines the Gaussian function.

$$g(x,y) = \frac{1}{2\pi\sigma^2} e^{-(x^2+y^2)/2\sigma^2} \tag{4.1}$$

where x is the distance from the origin on the horizontal axis, y is the distance from the origin on the vertical axis, and σ is the standard deviation of the Gaussian distribution. The 2D J_c image can be shown significantly detailed information more clearly so the gaussian filtered images of the defect region and normal region with a reasonable standard deviation, σ (=3). The normal region image with and without the filter is shown Fig 4.7 (a) and (b). After being applied filter to J_c image, the corresponding normalized I_c along the length obtained is shown in Fig 4.7(c). In addition, the statistical distributions of normalized I_c of normal regions can be seen in Fig. 4.8. It indicated the distribution as intrinsic I_c fluctuation in the normal region, which may come from the matrix itself. Hence, we identified the defect region by considering wider distribution of I_c than the three-standard deviation, $3\ \sigma$ (0.98 of normalized I_c) as the criterion. In the case of defect image shown in Fig. 4.9, the defect region was 11 mm along the length.
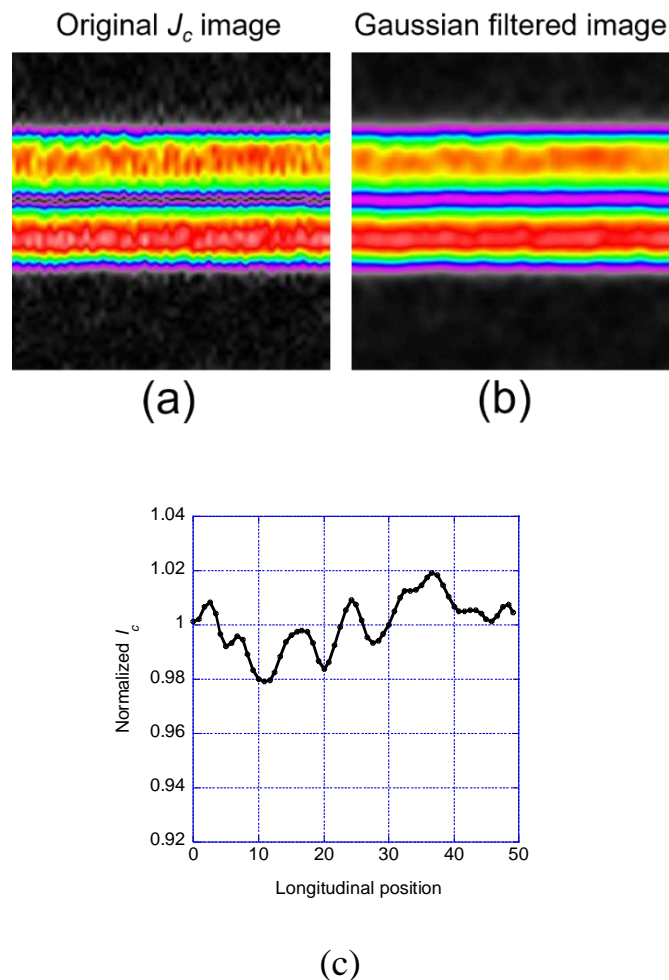

Fig. 4.7 (a) the normal image without filter, (b) After being applied filter to J_c image, (c) the corresponding normalized I_c along the length
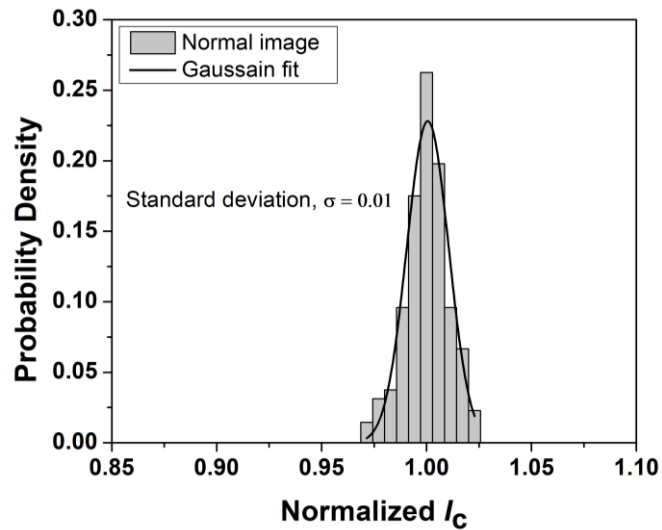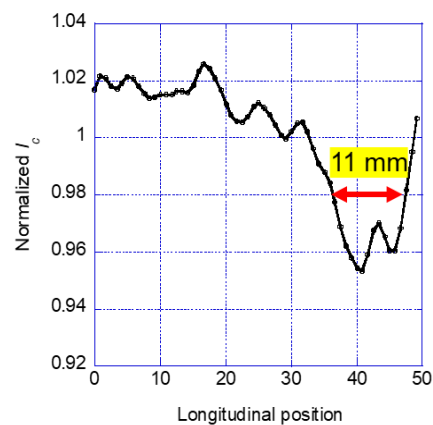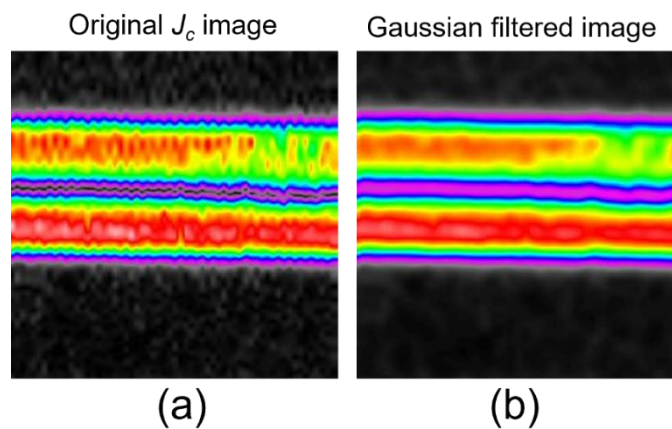
Fig. 4.8. Histogram with the probability density of normalized I_c distribution of sampling normal region

Fig. 4.9 (a) the defect image without filter, (b) After being applied filter to J_c image, (c) the corresponding normalized I_c along the length, showing size of defect

In this study on different defect sizes, we decided to split the defect sizes into three categories: large, medium, and small, and the original normal one. There are 40 images, 57 images, 89 images, and 100 images for large, medium, small and normal categories, respectively, so these images were used in the training data set to build multiple classifications. After measuring the defect region, the range of defect size was considered using the distribution of defect size fitted by Gaussian function, as shown in Fig. 4.10. The normal curve can determine the mode, mean and standard deviation, σ in order to estimate the defect size in each category. The small, medium and large size are 7.1 ± 1.2 mm, 12.7 ± 3.5 mm, and 21.8 ± 5.8 mm, respectively. The example of J_c images in four categories is shown in Fig. 4.11.
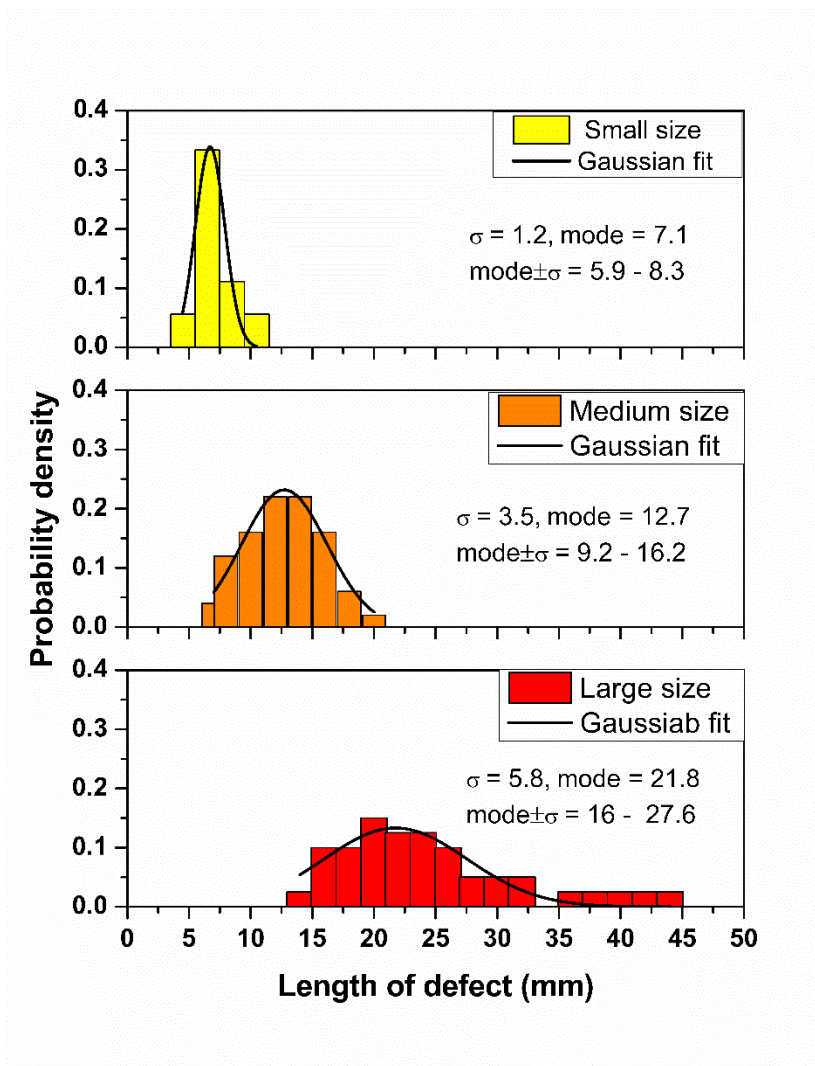

Fig. 4.10. Histogram with the probability density of size distribution of three defect categories
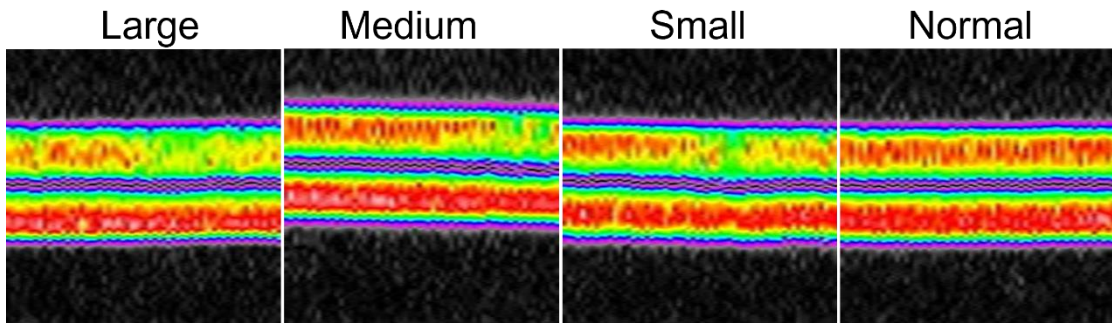
Fig. 4.11 The example of J_c images of four categories

4.2.2 Performance of model

The training data was split between a training dataset (80%) for training and a testing dataset (20%) for validation. In Fig. 4.12, the multiple image classification model reached the accuracy of 91% with loss value of 0.03 at the end of the 1500 iterations of the training process, which could be shown the high reliability for the classification. Meanwhile, in Fig. 4.13, the confusion matrix is displayed that the precision and recall of defects in the true and predicted class. The diagonal cells from top-left to bottom-right were highlighted with high accuracy shown as this model could classify these kinds of defects from J_c images with more correct and confidence at least 71% in each class of defect.
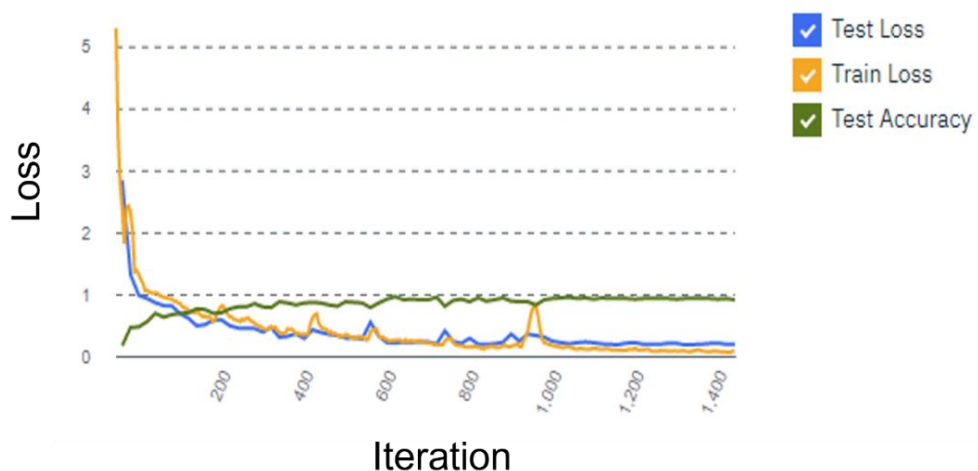

Fig. 4.12 Graph of loss and accuracy vs. iterations during training process of Model 2
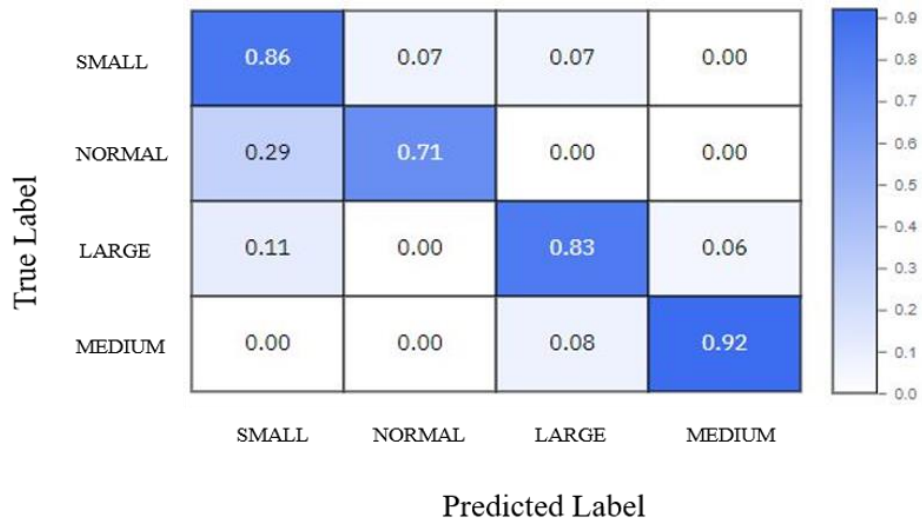
Fig. 4.13 Confusion matrix for the multi-class image classification model

4.2.3 Classification result

The four different categories can classify the defect sizes depending on the criterion for training defect size. The typical example of categorized three different defect sizes is shown in Fig. 4.14. The classification result conforms that the defect sizes are in the range of 3 different sizes based on training conditions. Whenever the size is closed to another category in between, the model provides the reasonable result with slightly less confidence.
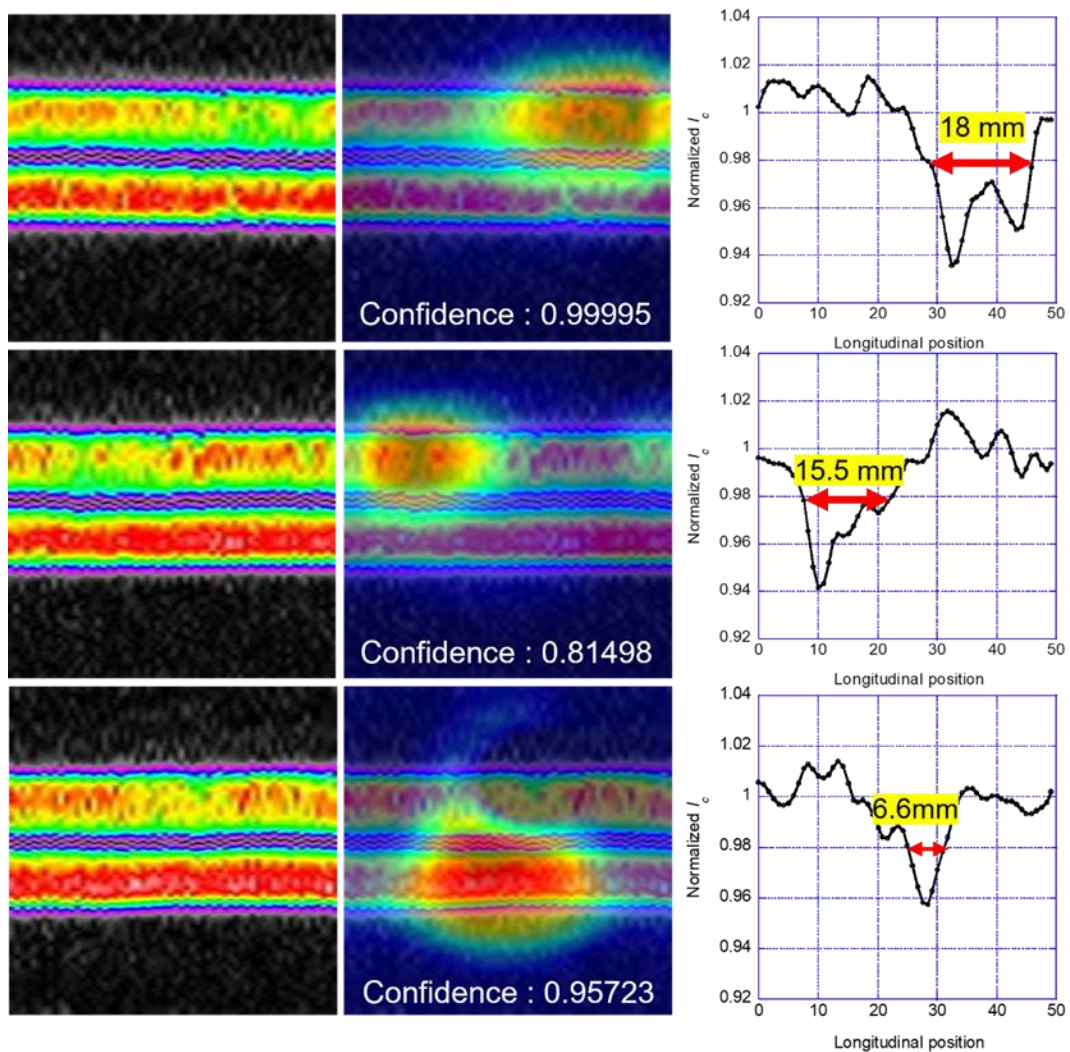
Fig. 4.14 The typical example of 3 different defect sizes in each category

The 4047 J_c pictures along the long CC categorized into four categories: large, medium, small, and normal regions were 195 images, 501 images, 1594 images and 1757 images, respectively. Then, this amount of defect and normal images vs the local $I_{c,min}$ value is shown in the distribution in Fig. 4.15. It indicated that distribution of defects can express the different sizes based on the criterion at training conditions. The distribution of large and medium sizes covered the statistical distribution of initial defects identified in the previous model having a binary state between normal and defect categories. In contrast, the small defect size might be between normal and defects found at a high value of I_c. It means that this model relatively provides a reasonable classification result due to defect and normal that are not sharply separated but

gradually instated. As a result, large and medium were considered critical defects and agreed with the prevised binary classification model.
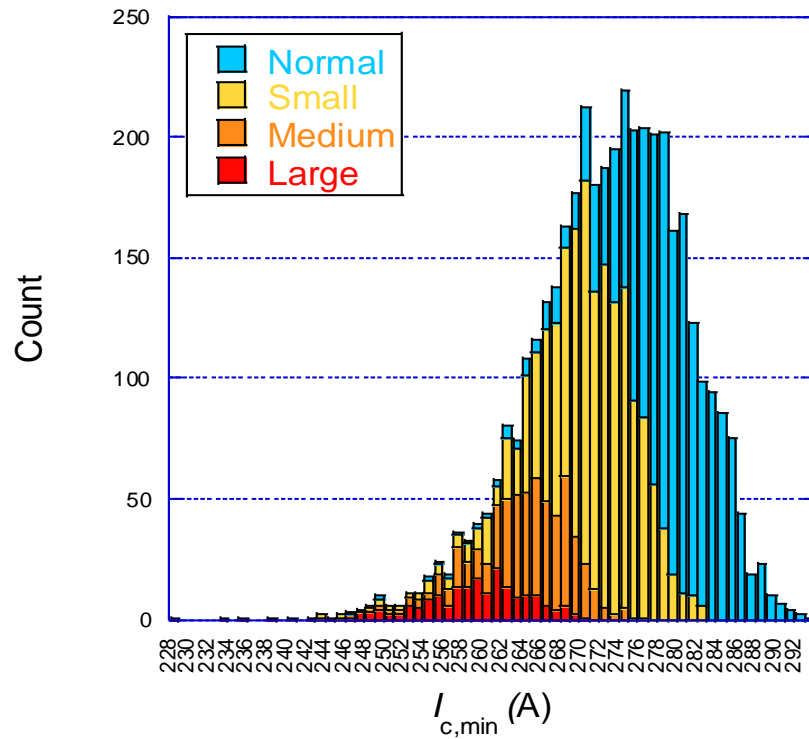

Fig. 4.15 The local $I_{c,min}$ distribution of all images after being classified into four categories

4.3 The applicability of the image classification model to sample made by same process from difference manufacture

4.3.1 Classification result

Another sample from commercial tape was used for assessing of the accuracy of the image classification model. The specification of the investigated commercial long tapes is illustrat in Table 4.2.

Table 4.2 The specification of the investigated commercial long tape

Manufacturer		SuperOx
Specification	Fabrication process	IBAD/PLD
	Width [mm]	4
	Length [m]	148
	Total thickness [μm]	60-100
	Rare earth	Gd
	Substrate	Hastelloy C-276
	Substrate thickness [μm]	60
Performance @77K, SF	I_c [A] guaranteed	>130

The 2D J_c mapping images were taken every 5 cm in longitudinal direction and composed of 2953 images along the length. The defect region and normal region could be classified into defect image and normal image class well. The critical example of them is shown in Fig. 4.16. It indicated that the image classification classified well with the J_c image obtained the CC made from difference manufacture and provided a reasonable heat map as well as high confidence score.

The classification model classified 247 images and 2706 into the defect and normal categories. It indicated that 8.36% of all images along the length were the defect regions that referred to the frequency of the local defect located at least 1-2 defects per 1m-length. The distribution of defect images vs local $I_{c,min}$ can be seen in the semi-logarithmic plot in Fig. 3.17.
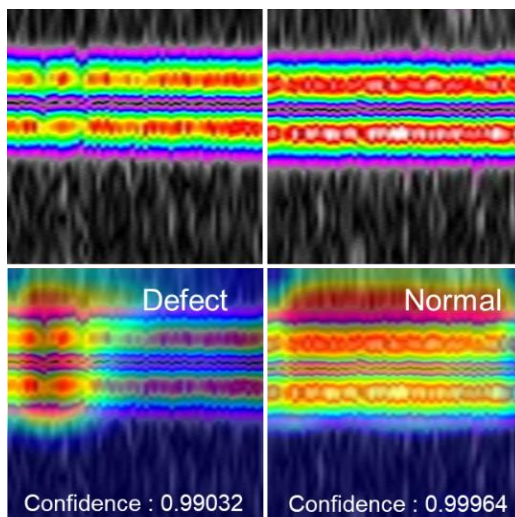
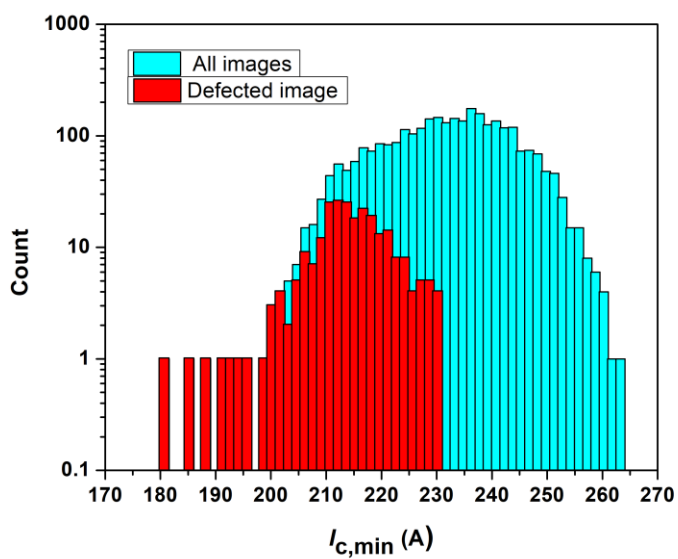Fig 4.16. Example of image classified to defect and normal category

Fig. 4.17 Histogram with the probability density of local $I_{c,min}$ distribution of defect images.

4.3.2 Comparison of the classification results of 2 tapes fabricated by IBAD-PLD process

The two commercial tapes fabricated IBAD-PLD process are illustrated in Table 4.3. They were classified to defect and normal images using the same classification model. The result of sample A and sample B are describe in section 3.4 and 4.3, respectively.

Table 4.3 the investigated two commercial long tapes

Sample	Fabrication process	Rare earth	Substrate	Width [mm]	Length [m]
A	IBAD/PLD	Gd	Hastelloy C-276	4	200
B	IBAD/PLD	Gd	Hastelloy C-276	4	148

In order to compare between 2 tapes, the distribution of local $I_{c,min}$ need to normalize by an averaged I_c value, and a comparison of normalized I_c of defect category between 2 tapes is shown in Fig. 4.18. The statistic distribution of I_c regarding defect region was 9.20% in sample A and 8.36% in sample B. Boths indicated the group in the lower I_c distribution dominated by extrinsic defects, whereas a comparison of I_c normalized distribution of normal categories is shown Fig. 4.19, indicating the homogeneity of the intrinsic matrix. In addition, the standard deviation of each distribution is illustrated in Table 4.4. As a result, the standard deviation of normal category clearly indicates that PLD process itself was superior in the case of sample A showing a lower value than in sample B, even though the probability of a defect in sample B is slightly less. It suggests that if sample B improves PLD process as good as in the case of sample A, the I_c homogeneity and quality will be improved significantly.
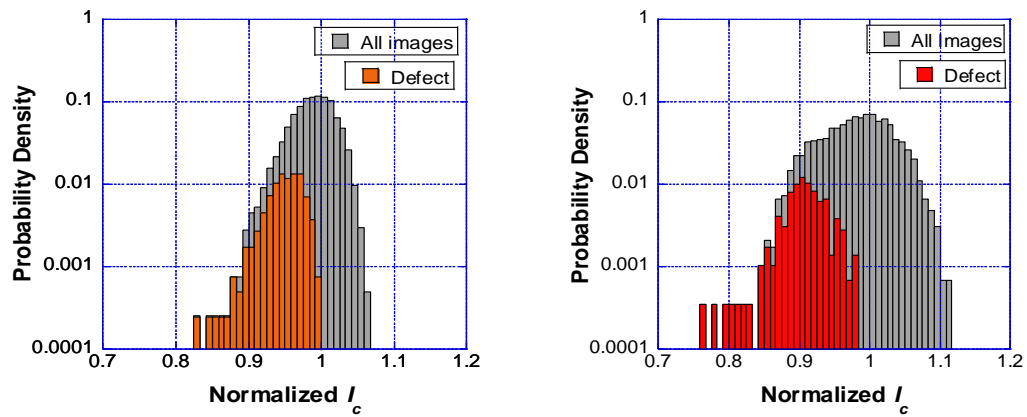
Fig. 4.18 Comparision of normalized Ic of defect category between 2 tapes.
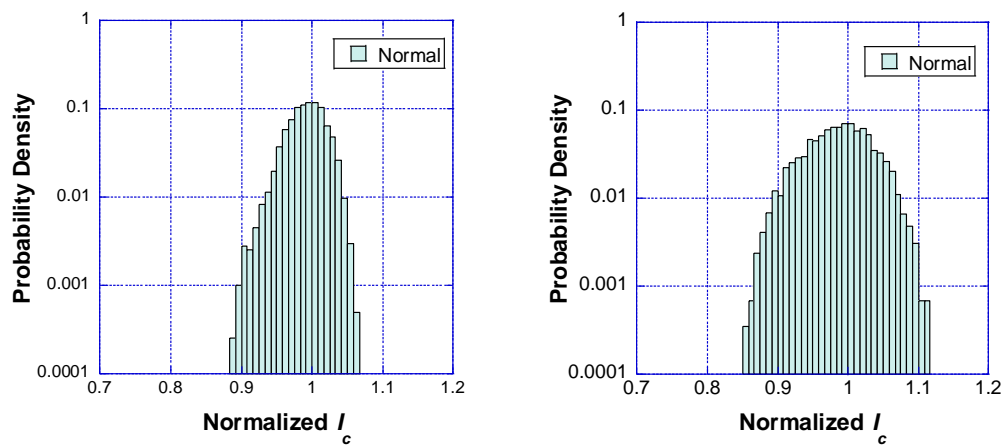

Fig. 4.19 Histogram in semi-logarithmic scale with the probability density of normalized I_c categorized into normal category.

Table 4.4 The standard deviation of each distribution from investigaed 2 samples.

	Standard deviation	
Sample	Fujikura(A)	SuperOx(B)
All	0.2865	0.3005
Defect	0.2714	0.2584
Normal	0.2466	0.2650

4.4 The further extension to the other processes such as MOD, MOCVD, RCE-DR

In this section, we investigated the inhomogeneity of commercial coated conductors made from different fabrication routes by adopting the image classification model to recognize the local obstacle in magnetic images visualized by the RTR-SHPM system and the statistics of local obstacles were studied.

4.4.1 Sample

The characteristic of the investigated commercial coated conductor from four different fabrication processes is present in table 4.5.

Table 4.5 Detailed information of the investigated samples.

Sample	Fabrication process	Rare earth	Substrate	Width [mm]
A	RABiTS/MOD	Y	Ni-5W	4.4
B	IBAD/RCE-DR	Gd	Hastelloy C-276	4.1
C	IBAD/MOCVD	Y,Gd	Hastelloy C-276	4
D	IBAD/PLD	Gd	Hastelloy C-276	5

The commercial REBCO coated conductors were developed for both in-plane and out-of-plane texturing of superconducting layers on the biaxially textured alignment of substrates deposited by two techniques: ion beam-assisted deposition (IBAD) and rolling-assisted biaxially textured substrates (RABiTS). The epitaxial superconducting layer is deposited either by chemical routes, such as metal organic deposition (MOD) [15] and metal organic chemical vapour deposition (MOCVD) [16], or by physical routes, such as pulsed laser deposition (PLD) [17] and reactive co-evaporation (RCE) [18].

4.4.2 Comparison of the classification results of 2 tapes fabricated by IBAD-PLD process

The RTR-SHPM system was used in measuring the distribution of the magnetic fields above the surface of four samples in a remanent state by a Hall sensor across the width direction, as the tape was moving in the longitudinal direction along 18.5 m the CCs under a liquid nitrogen temperature of 77 K. Then, by solving the inversion problem of Biot-Savart law, the corresponding magnetization was obtained. The sheet critical current density of four samples is shown in Fig 4.20, indicating the sample D is relatively high compared with the other samples as well we the inhomogeneity in distribution appear periodically. Moreover. It is roughly noticed that the IBAD/MOCVD technique provide the homogeneity of the CC.

However, based on our image classification, these J_c distributions used as the 2D images were taken every 5 cm in a longitudinal position and the images needed to be normalized by average J_c in each 5 cm section due to the lever of critical current density that was different from one another, Then, they were suitable for the image classification model.
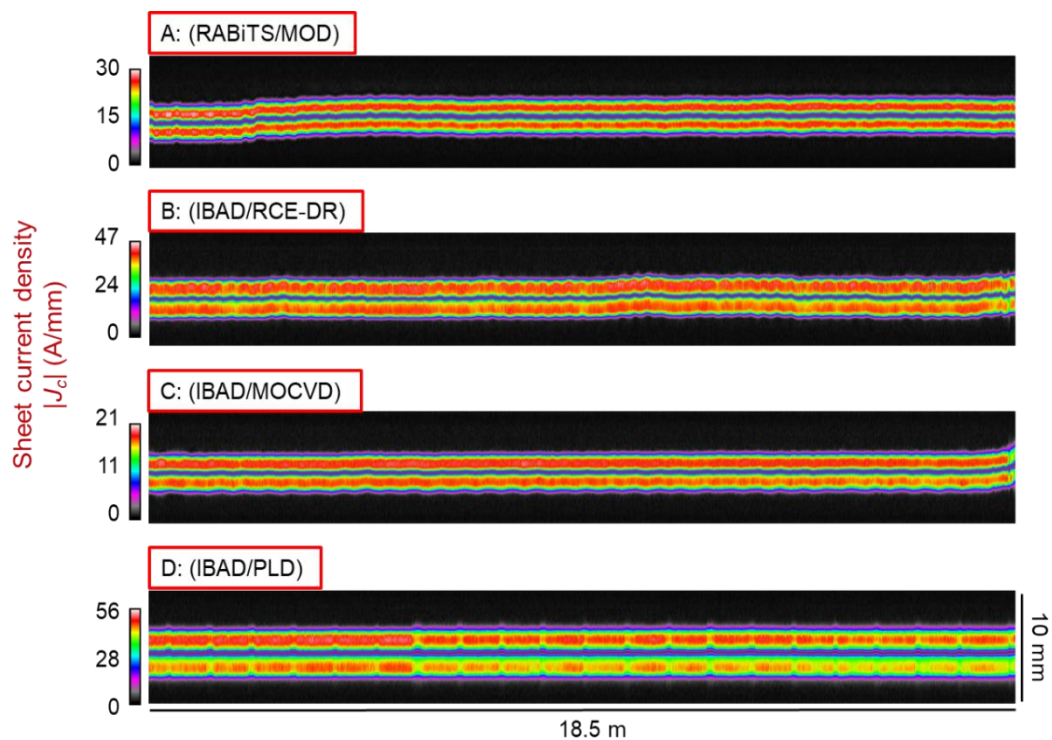

Fig. 4.20 Critical current density in coated conductors from different fabrication processes characterized by RTR-SHPM

4.4.3. Classification result

In detection analysis, the model could identify the defect detection discovered in all samples after the images were put into the classification, as shown in Fig. 4.21(a). It detected very well with greater confidence of 0.9, as well as a heat map related to its site. The defect region indicated magnetization drop resulting in I_c degradation. It noticed that the kind of defect was relatively similar in each sample and familiar with the defect found in CC fabricated by the IBAD-PLD process, which was the data set for the training image. Meanwhile, the defect image was discriminated from the normal image showing the corresponding whole heat map with the high confidence. The normal image is shown in Fig. 4.21(b).
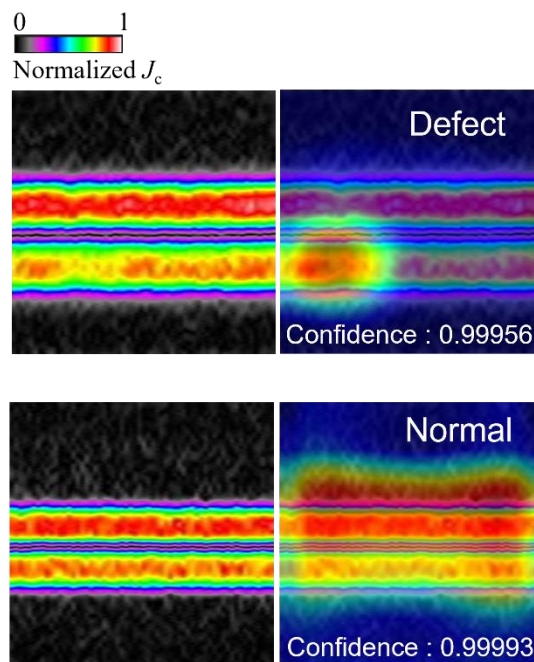

Fig. 4.21 Example of defect and normal image is found in four tapes.

However, in order to evaluate the applicability to four different tapes, the number of correct and incorrect classifications was used in the confusion matrix to evaluate the performance. These performance evaluations can be seen in Table 4.6.

Table 4.6 The evaluation matrices of the original model.

Sample	Classification result				Recall	Precision	Accuracy	F1
	TP	TN	FP	FN				
A	7	357	3	3	0.70	0.70	0.98	0.70
B	9	348	5	8	0.53	0.64	0.96	0.58
C	3	367	0	0	1	1	1	1
D	24	338	2	6	0.80	0.92	0.98	0.85

Abbreviations: true positive (TP) means that the image is correctly identified as a defect image, true negative (TN), means that the image is correctly identified as a normal image, false positive (FP) means that the normal image is wrongly identified as defect image, and false negative (FN) means that the defect image is wrongly identified as a normal image.

Based on the information of these evaluation matrices, it shows that samples A, C, and D is reasonably good recognition rates with the F1-score of more than 0.7, allowing this classification model to be used, whereas sample B was recognized as the defect image with a lower recognition rate with F1-score of 0.58 due to missing half of the number of an actual defect image.

In order to investigate the reason why the sample B has lower performance on the classification in this model, we studied J_c images and found that the defect position could not defected this model. It interprets this defect type in sample B as a normal image, as shown in Fig. 4.22. This defect has the sharp magnetization drop around the shape of the defect position. Simultaneously, the model responded appropriately by using a heat map to avoid the defect region.
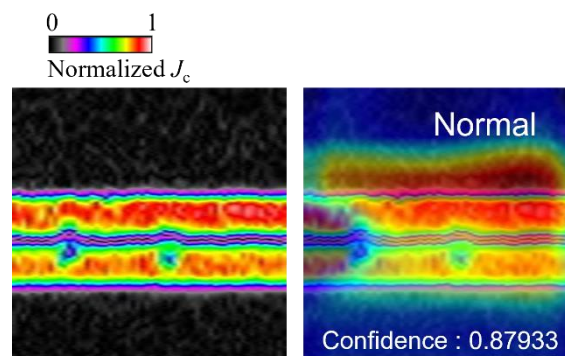

Fig. 4.22 The defect image from the sample B could not be correctly classified by the classification model.

To further improve the model applicability, we added a few training defect images taken from sample B. After a bit of improvement, the performance evaluation is illustrated in Table 4.7.

Table 4.7 The evaluation matrices of the improved model.

Sample	Classification result				Recall	Precision	Accuracy	F1
	TP	TN	FP	FN				
A	7	358	2	3	0.70	0.77	0.98	0.73
B	14	346	7	3	0.82	0.67	0.97	0.74
C	3	367	0	0	1	1	1	1
D	25	337	3	5	0.83	0.89	0.98	0.86

The improved model could increase F1 by 16 % in sample B as well as the model can classify the defects well in each tape without the degradation of the performance on classification. The example of the test image for the improved model compared to the original model is shown in Fig. 4.23, indicating that the model provides a satisfactory result with the corresponding heat map as well as high confidence score. That means that the improved model was able to enhance the correctness by training with a variety of defect types that depended on different processes and was applicable to recognize two defect types in at least four combinations of the processes.
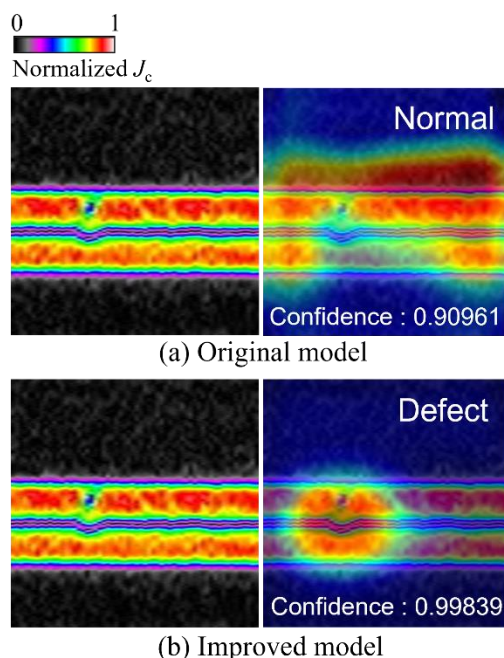
(a) Original model

(b) Improved model

Fig. 4.23 Comparison of test image classified by classification model between the original and improved model. (a) The original model does not correctly classify the defect image from the sample B. (b) The improved model could correctly classify the defect image.

4.4.4 Evaluation of longitudinal I_c distribution in the HTS tape based on image classification

We investigated the influence of local obstacles in sample B on the critical current along the 18.5-m length to demonstrate the capability of this image classification. Fig. 4.24(a) shows the I_c variation as a function of longitudinal coordinate by integrating the local sheet current density across the width obtained by RTR-SHPM. The local I_c drops over 14 defect images were shown and pointed out by a red dot. After these detect images noticed the position of local obstacles by image recognition, the local I_c drops due to the existence of obstacles were crossed out, and the homogeneity of I_c variation can be shown in Fig. 4.24(b). Based on this advantage, the local I_c distribution along the defect images in sample B was extracted from the overall I_c distribution along the length, and it can be seen by a histogram with the semi-logarithmic scale in Fig 4.25(a). It noted that this distribution was the double

distribution that originated both at lower I_c distribution corresponding to local I_c drops due to the obstacles in tape and high I_c distribution from the normal region. Consequently, we can estimate the single distribution at a high I_c value after taking into account the normal image, excluding the influence of local obstacles, as shown in Fig 4.25(b).
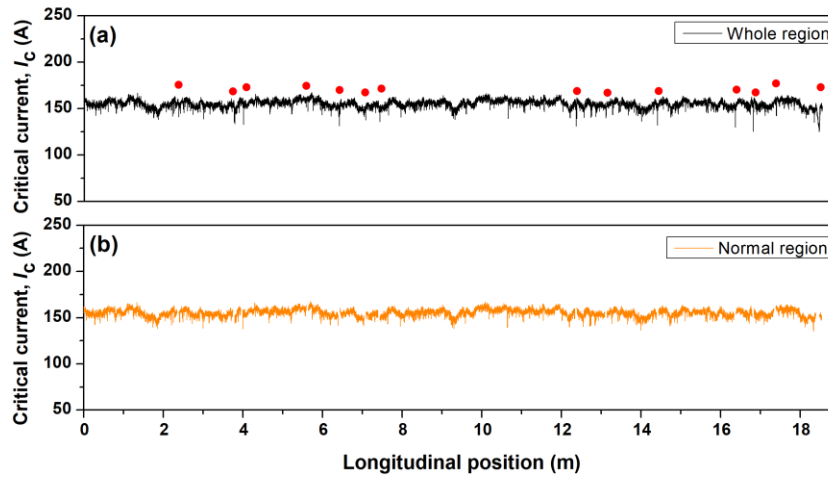

Fig. 4.24 Longitudinal variation of local I_c in the sample B. (a) original I_c along the whole length, including red dot pointed out local I_c drops related to defect images (b) Normal region without defect images removed based on information from image classification
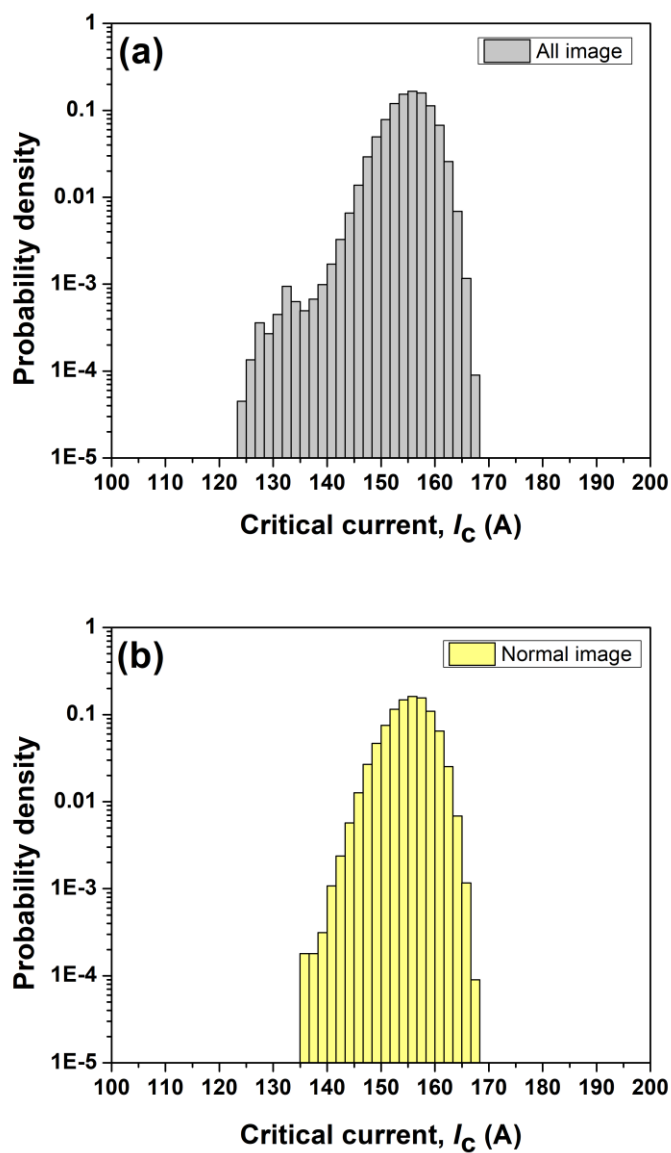
Fig. 4.25 Histogram with the probability density of local I_c distribution in sample B segregated defect image from normal image by image classification (a) defect image (b) normal image

Chapter 5

Object detection for recognizing defect in HTS tapes

Based on previous classification results, the model succeeded in classifying the defect region, types of defects and the size of defects roughly defined based on training size criterions. Thus, in this chapter, we introduced the deep learning-based object detection to the RTR-SHPM for characterizing advanced information of the local obstacles such as size, position, and statistic defect behavior according to the advantage of object detection, which is combination of image classification and object localization.

5.1 Overview of object detection

The object detection algorithm has been developed and carried out on convolutional neural network (CNN). The CNN architecture from image classification is used to extract features from images for all the regions of interests (ROIs) in the image. Then, the bounding box Regression is directly added to the CNN network for training where to look or pay attention to the positioning each ROI. Finally, the system performs classification and regression on region proposal to gather bounding boxes with scores for each class. Based on this explanation, this algorithm is known as the R-CNN algorithm based on Region Proposal, such as R-CNN, Fast R-CNN and Faster R-CNN [51], [52]. In this research, The Faster Regional Convolutional Neural Network (Faster R-CNN) model providing high efficiency in object detection field is implemented So, object detection combines image classification and localization. It is used to identify the location of objects in an image showing a bounding box around those desired objects.

5.2 Building object defection model

5.2.1 Data preparation for training set

As describe in the section 4.2, By making the local average value in space by applying Gaussian filter, the 2D J_c image can be shown significantly detailed information more clearly as well as the corresponding normalized I_c over the length could also identify the defect region due to wider I_c fluctuation as extrinsic than normal intrinsic one. That means the defect regions were related to extrinsic defects having standard deviation of more than 0.01 observed normal curve of I_c from normal region.

In Fig 5.1, we precisely decided the boundary of detects in the original J_c image by drawing a rectangular box around a magnetization current drop lower than neighboring normal region. The J_c images containing the existence of local defects were gartering for the training data set needed to train the model. There were 19 labelling as a defect that was used to train the model. The labelled box named defect give the coordinates of the defect where it is in that image. The labelling is only required when we are doing object detection to precisely teach the localization of the object.
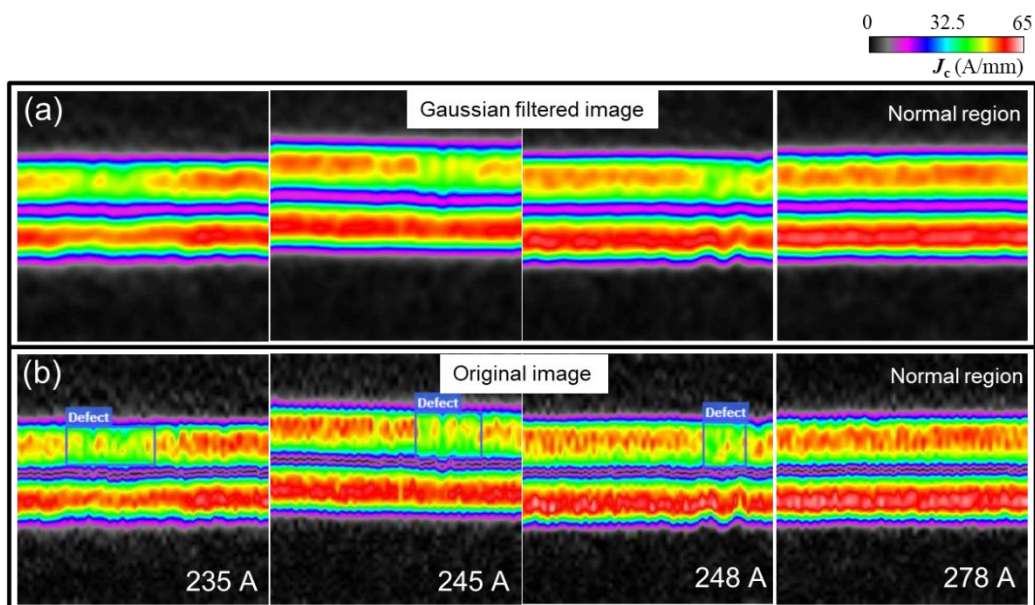

Fig. 5.1 The example of J_c mapping images containing with or without defects (a) gaussian filtered images (above) and (b) labelled defect images for training data set, including local minimum critical current, $I_{c,min}$ in each image (below)

5.2.2 Performance of object detection model

The model was trained on based Faster R-CNN architecture. The training data was sent to train the training algorithm at a maximum of 4000 iterations with a learning rate of 0.001 and weight decay of 0.0005 to minimize the loss function and reduce the error during the training model. The default ratio value of the training data was 0.8 resulting in spiting 80% and 20% of the images for training, and validation, respectively. As a result, this model is good learning and performs with 100% accuracy with the selected parameters, and the relative performance of the training model over time shows the convergence at the end of training loss of classification and training loss of bounding box prediction with 0.02 of error as shown in Fig 5.2, indicating the reasonable training object defection model made up of classification and localization of object in image detected by bounding box prediction. Under object detection evaluation metrics, the bounding box prediction and ground-truth bounding box (i.e., hand labeled) are compared the area of overlap between the predicted bounding box and the ground-truth bounding box divided by the area of union between them, which is intersection over union (IoU) used as de facto evaluation metric in object detection. When evaluating object detection algorithms, an IoU threshold of more than 0.5 is typically used to determine whether a detection was correct [51], [53]. At the end of training object algorithm, this model had good detection with an IoU score of 0.76 that was highly reasonable value reported in [53].
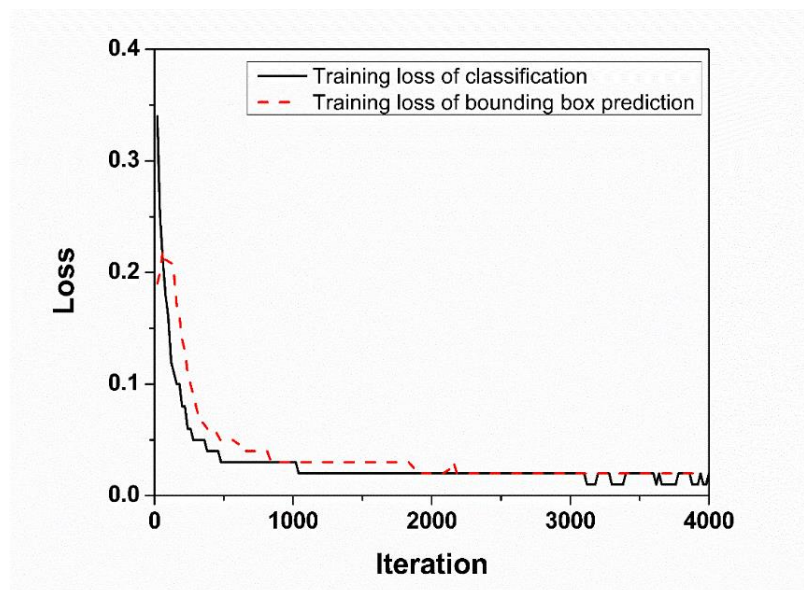

Fig. 5.2 Graph of loss and Accuracy vs. iterations during training process of the object detection model

5.3 Defect recognition in the long commercial REBCO tape

5.3.1 Defect recognition results object detection

Fig. 5.3(a-1) shows the J_c mapping images containing the local defect recognized by the object detection. The rectangular box surrounding the localized drop in the magnetization current indicates the existence of a microstructural defect. The position of the rectangular box shows good agreement with the local I_c drop at 262 A, where the degradation of I_c as a function of longitudinal position occurred, as shown in Fig. 5.3(a-2), indicating that the fluence of local obstacles was able to be estimated from the bounding box. Even though, in the case of local I_c drop at a high I_c region where I_c drops still carried high capability, object detection could detect, as shown in Fig 5.3(b). Besides, considering I_c fluctuation as the conventional method is not easy to identify these local obstacles due to both extrinsic defects and intrinsic distribution in the matrix itself. As a result, we can easily recognize the obstacles from J_c mapping image and extract detailed information such as position, I_c over defect region.
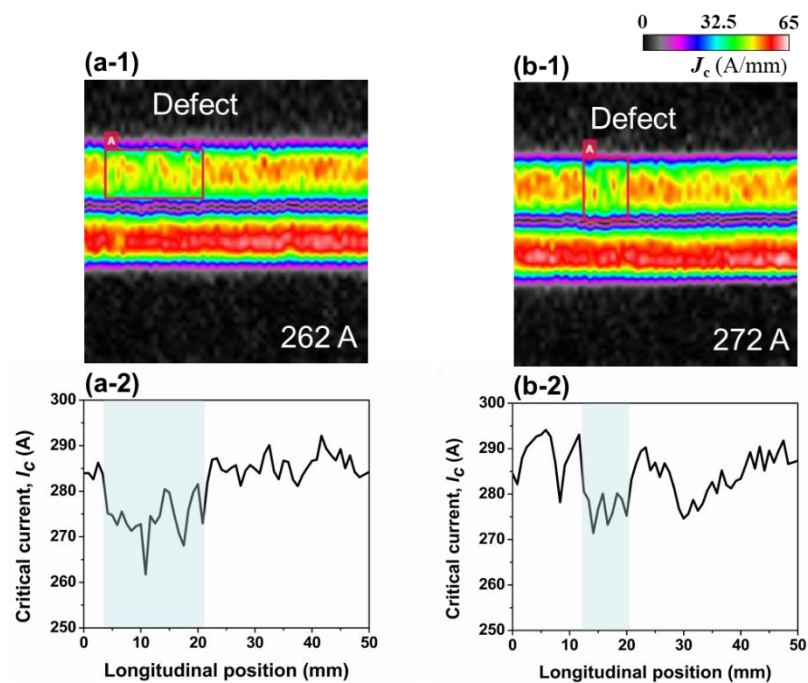

Fig. 5.3 Result of defect detection result and corresponding I_c long the longitudinal position. (a-1) J_c mapping image recognized the defect at $I_{c,min}$ = 262 A, (a-2) corresponding I_c (b-1) J_c mapping image recognized the defect at $I_{c,min}$ = 272 A and (d)) corresponding I_c

5.3.2 The statistical distribution of critical current

The examined 1-m CC in longitudinal I_c distributions generated by RTR-SHPM is shown in Fig. 5.4. Using deep learning-based object defection, the local I_c drops corresponding to the influence of the obstacle were extracted from normal I_c fluctuation as intrinsic fluctuation. We assumed that local I_c homogeneity was obtained after removing the influence of microstructural defects on local I_c along the tape in order to explore the qualities because we can now track down the local obstacle in tape.
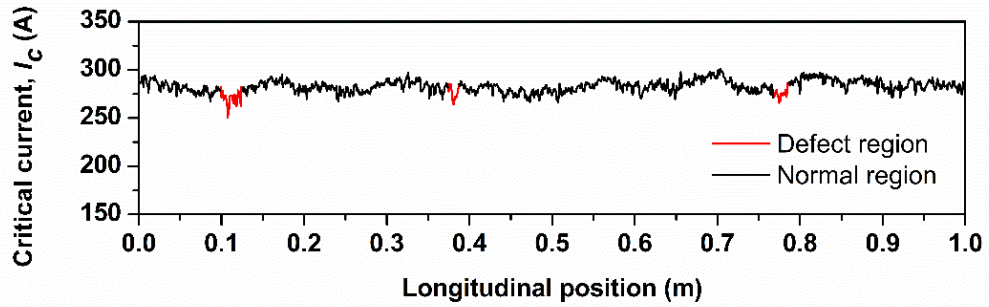
Fig. 5.4 The examined 1 m CC in longitudinal distributions of I_c obtained by RTR-SHPM

By applying object detection to the total length, there were the detected 747 obstacles or at least 3 obstacles per 1m-length and the local I_c corresponding to defect region and normal along the 200 m-long CC was studied the statistical I_c distribution of defect and normal region. The I_c distribution of all defect regions shows in a histogram with the probability density by liner scale Fig. 5.5(a). It indicated that 6.36 % out of the total I_c was influenced by obstacles. The probability density of statistical I_c distribution can be seen in the semi-logarithmic plot, and the investigated properties of the CCs can be described as the asymmetry distribution due to the influence of intrinsic and/or extrinsic defects using Weibull function [54]. With three Weibull parameters, the probability density of the critical current is expressed by

$$P(I_c) = \left(\frac{m}{I_{c0}}\right)\left(\frac{I_c - I_{cm}}{I_{c0}}\right)^{m-1} \exp\left[-\left(\frac{I_c - I_{cm}}{I_{c0}}\right)^m\right] \qquad (5.1)$$

Where, I_{cm} is the minimum lower limit critical current, I_{c0} is the scale parameter, and m is the shape parameter.

Fig. 5.5(b) shows the probability density of I_c distribution of defect region and the overall I_c distribution in histogram with the semi-logarithmic scale. The distribution of the overall I_c, which came from intrinsic and extrinsic fluctuation, was described by Weibull fit-1 with $I_{cm} = 206$ A, $I_{c0} = 83$ A, and $m = 12$, while Weibull fit-2 separated the distribution of the defect region with $I_{cm} = 201$ A, $I_{c0} = 77$ A, and $m = 12$, indicating that distribution shifted to lower I_c value due to including the influence of extrinsic defect in tape. Furthermore, the normal distribution of I_c estimated from the normal region in the tape, which was not detected as the defect by the object detection shown in Fig 5.5(c). This distribution was fitted by Weibull fit-3 with $I_{cm} = 216$ A, $I_{c0} = 74$ A, and $m = 12$. It noticed that the distribution of I_c is significantly narrower than its original one with decreased I_{c0} by 6 A and increased I_{cm} value. As a result, we can estimate the double distribution coming from different magnesium, such as intrinsic and extrinsic defects.
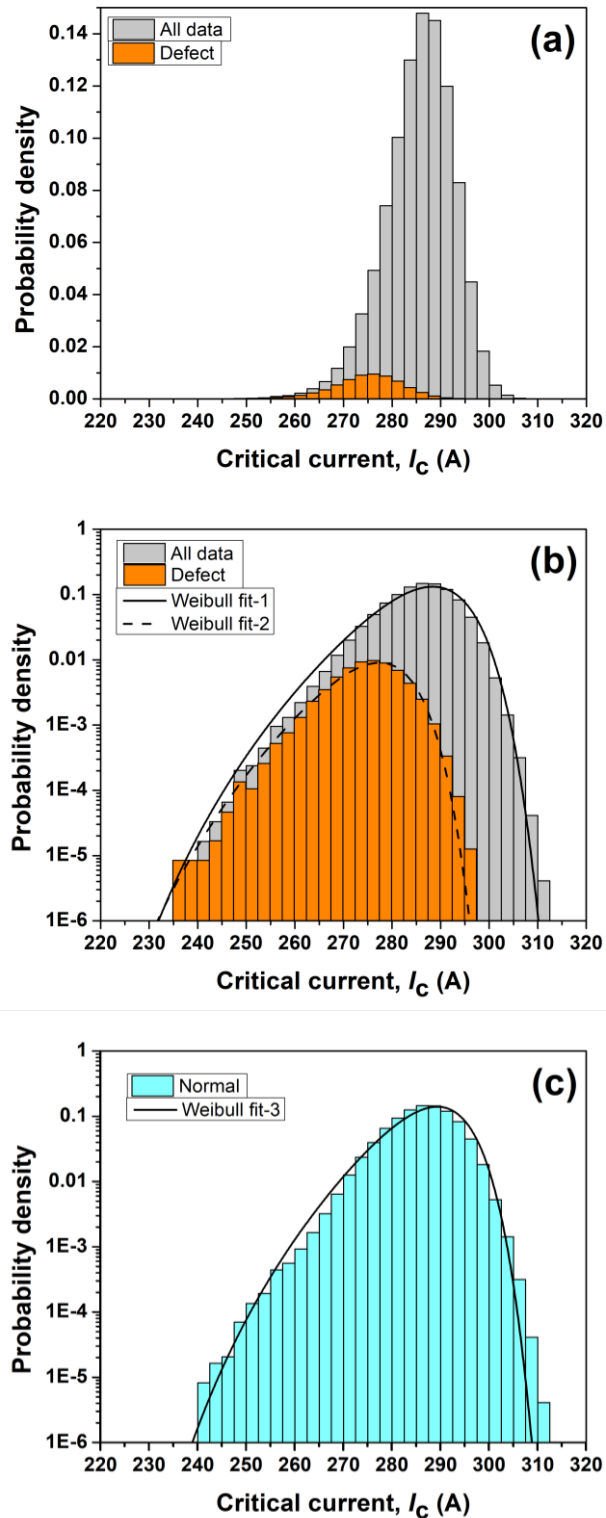
Fig. 5.5 Histogram with the probability density of local I_c distribution of the CC categorized into defect and normal groups by the object detection (a) defect group shown by linear scale, (b) defect group by semi-logarithmic scale, (c) normal group by semi-logarithmic scale

5.3.3 Information extraction of size and generation frequency in the tape

(1) Relationship Between Defect Size and Normalized ΔI_c

This object detection detected total 747 defects throughout 200 m long CC. Based on this analysis, defect size depending on the low I_c region extending in longitudinal length was indicated by the length of the predicted bounding box, so the distribution of defect size is shown in Fig. 5.6. It indicated that object detection could approximately estimate the average defect size of 10.7 mm using Gaussian fit, but whenever defect size becomes smaller than 5 mm, the object detection could not detect because of the lack of spatial resolution of our measurement.
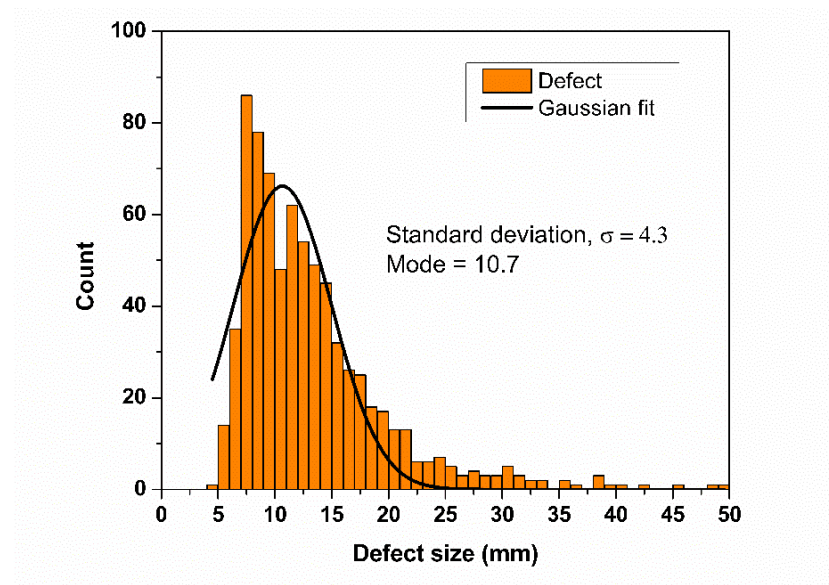
Fig. 5.6 Histogram with the probability density of size distribution

However, if we investigate the normalized ΔI_c of those defect regions detected by object detection and the other normal regions within 5-cm section based on object defection results, as shown in Fig. 5.7. The normalized ΔI_c of both regions is defined by the following equation (5.2) and (5.3).

$$normalized\ \Delta I_c = \frac{|I_{c,ave}^{*} - I_{c,ave}|}{I_{c,ave}} \qquad \text{(defect region)} \qquad (5.2)$$

$$normalized\ \Delta I_c = \frac{|I_{c,ave}^{**} - I_{c,ave}|}{I_{c,ave}} \qquad \text{(normal region)} \qquad (5.3)$$

Where, $I_{c,ave}^{*}$ is an average I_c in 5-cm over the defect and $I_{c,ave}^{**}$ is an average I_c in 5-cm normal region, excluding defect region and $I_{c,ave}$ is an average I_c from all normal regions along 200-m (747 images) and proportional to 282.77 A.
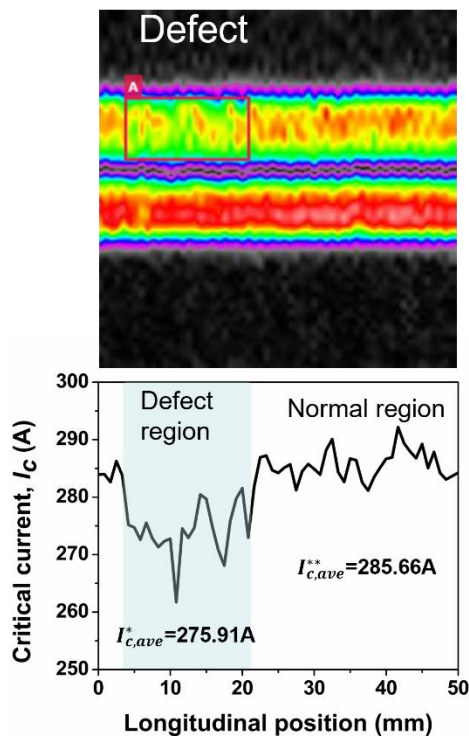

Fig. 5.7 The example of object detection result and the corresponding I_c in 5 cm, which is used for calculating an average I_c over defect region ($I_{c,ave}^{*}$) and an average I_c over normal region ($I_{c,ave}^{**}$).

The statistic normalized ΔI_c distribution of both regions shows similar gaussian behavior with different standard deviation, as shown in Fig. 5.8. Because of extrinsic effect, the ΔI_c distribution of defect region result is wider distribution than normal one. Based on these statistic distributions, it indicated that the rage of a smaller defect size than 5 mm has the distribution of normalized ΔI_c in the range defined by σ in the normal region. It means that the object detection could not define the background of defects because of scattering of I_c in the matrix itself. Moreover, it can be seen more clearly by checking the relationship between defect size and ΔI_c in Fig. 5.9. This relationship shows the linear relationship, which means the defect size depends on ΔI_c due to the current blocking effect [54]. It is noticed that the defect region has large ΔI_c

due to suppressing of I_c in the defect region, compared to the normal region at an average σ of 0.01.
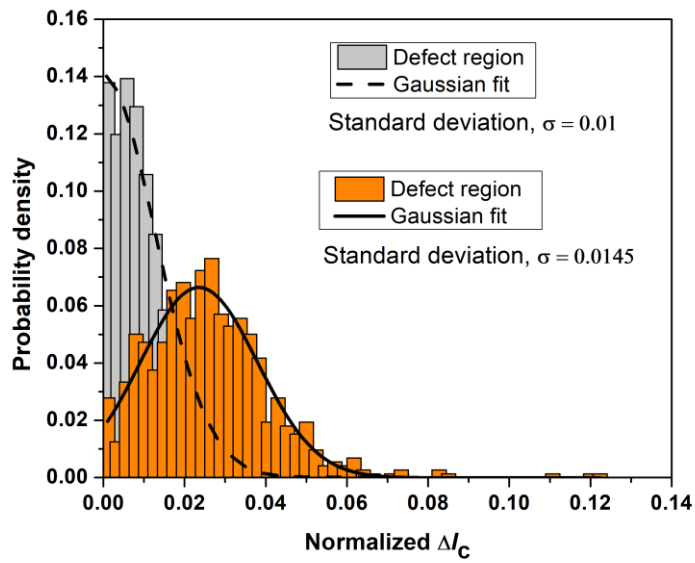

Fig. 5.8. The statistic normalized ΔI_c distribution of defect and normal regions
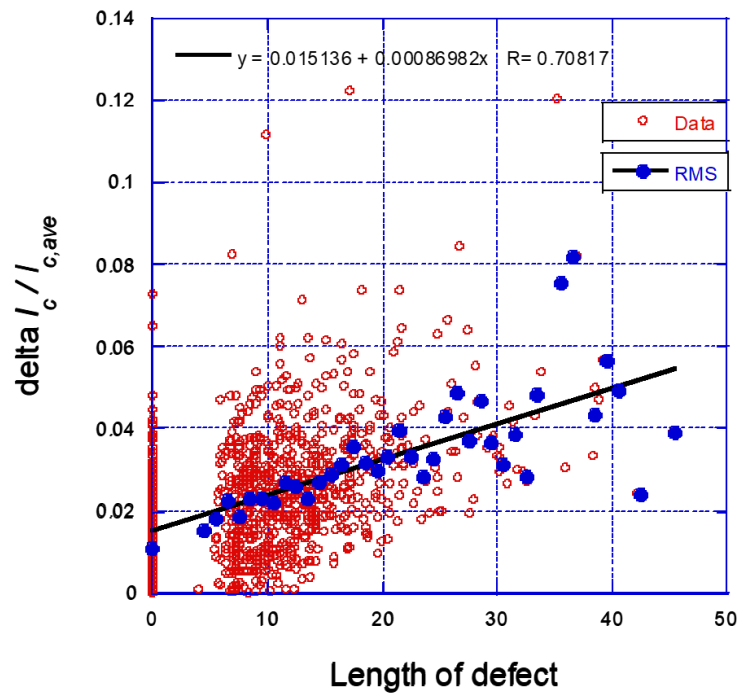

Fig. 5.9. The relationship between defect size and $\Delta I_c/I_{c,ave}$

(2) Fractal Behavior

Based on this information extraction from object defection, detect not only the obstacles but also extract additional information such as size and position. In previous discussion about size distribution indicated that the small size is at the top of the distribution that commonly appears in the tape, while the large defect significantly decreases in terms of occurrence. Moreover, the statistic distribution of occurrence of defect was helpful in investigating the superconducting properties. The position of defect in longitudinal position is shown in Fig. 5.10 indicating that the occurrence of the defects shows Fractal behavior, i.e., the occurrence of the defects is not random with a constant probability.

The distribution of the spacing between adjacent detects is shown in Fig. 5.11. It can be plotted on a double logarithmic scale as a function of probability density described well with a straight line by power law. As a result, power law behavior randomly originated the frequency of occurrence of local defects in the CC with fluctuated distance influenced by nature of factual behavior.
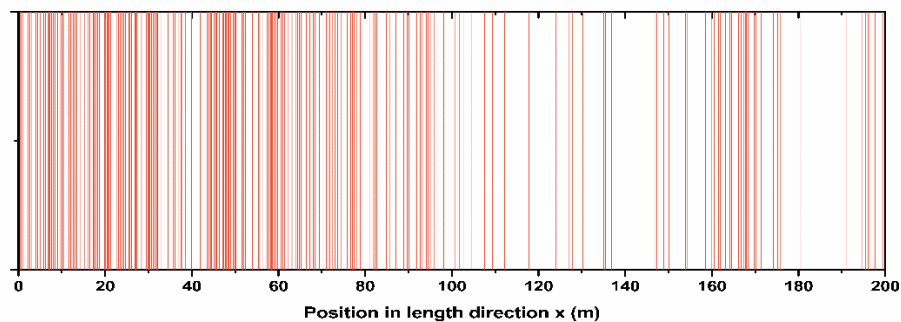

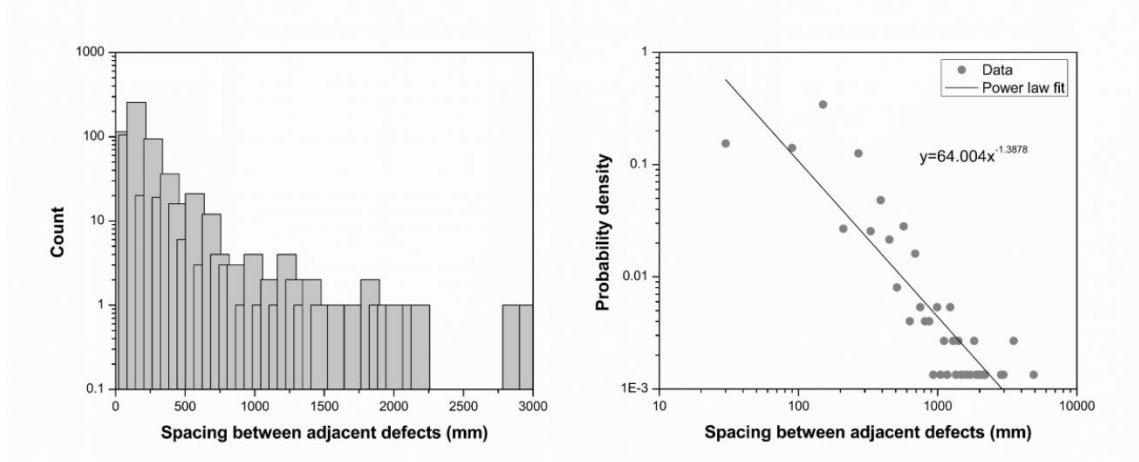Fig. 5.10 The position of defect in longitudinal position.

Fig. 5.11 The histogram illustrates the spacing distribution between adjacent defects (Lift) and the probability density of spacing between adjacent defects (right)
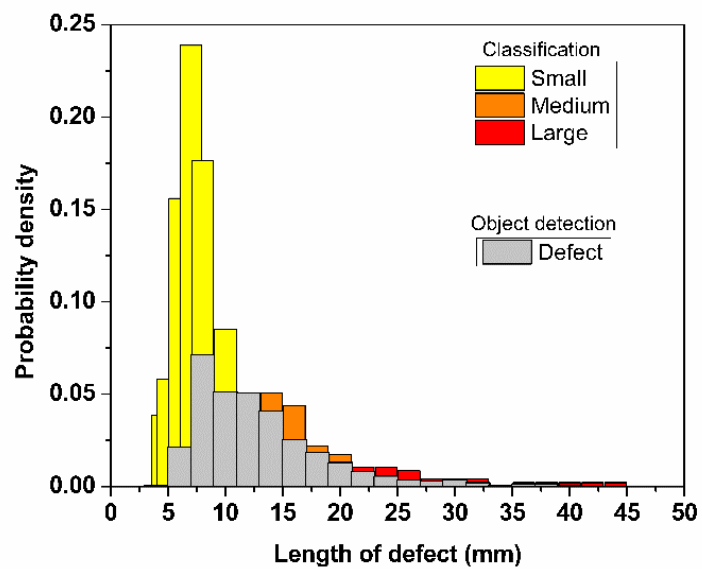
5.4. Comparison of defect size distribution between classification and object detection

From the results in section 4.2 for the image classification with multiple defect size categories, the defects were categorized into three levels based on the training size criterion. According to these results, we know the number of defects in each category. We then assume that the whole numbers are categorized into large, medium, and small sizes distributed within a normal curve evaluated by a training set, so the size distribution can be seen in the Histogram with probability density in Fig 5.12(a).

In order to support this assumption, we analyzed the same coated conductor tape by applying object detection in section 5.3.3. The number and size of defects were evaluated and compared with a classified size distribution, as shown in Fig. 5.12(b). The distribution of both methods is almost the same if we merely limit the number of defects categorized in large and medium sizes. They also show reasonable results, and we can even predict the size based on classification. According to the object detection results, the minimum defect size is around 5 mm and its statistical distribution shows good agreement with that of medium and large size defect categories obtained from the multiple classification. The defects in these size range may influence the local I_c drop, whereas the influence on the local I_c drop is the same order of intrinsic fluctuation in the small side defects categorized in the small sized defect in our classification model, i.e., less than about 5 mm.
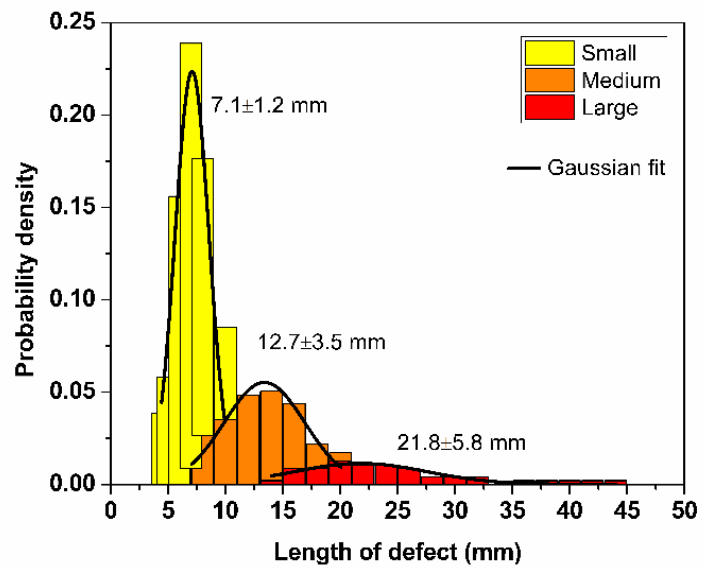
(a)

(b)

Fig. 5.12. Histogram with probability density of statistic size distribution evaluated by classification and object detection. (a) size distribution from classification. (b) comparison of size distribution between two methods

Chapter 6

Image pixel interpolation for image recognition

6.1 The advantage of Tapestar^{TM}

For the evaluation of longitudinal homogeneity in the CCs, Tapestar^{TM} technique is widely used for estimating of longitudinal distribution of critical local current (I_c) by measuring the penetrating gradient magnetic field across the width. The I_c calculated as the value is proportional to the root mean square the slope of the penetrating magnetic field, as described in chapter 2. The example of I_c variation along the 148 m-long coated conductor is shown in Fig. 6.1
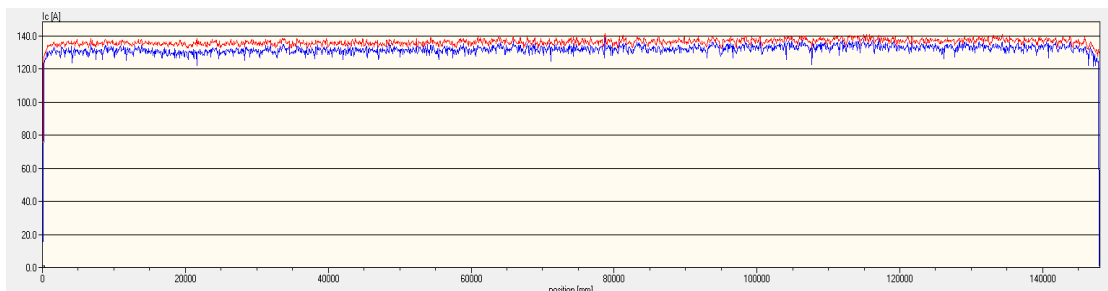

Fig. 6.1 The example of I_c variation along the 148 m-long coated conductor

Based on this advantage, the distribution of magnetic field penetration across the width was taken into account in 1D and 2D carrying in a continuous longitudinal position, as shown in Fig 6.2
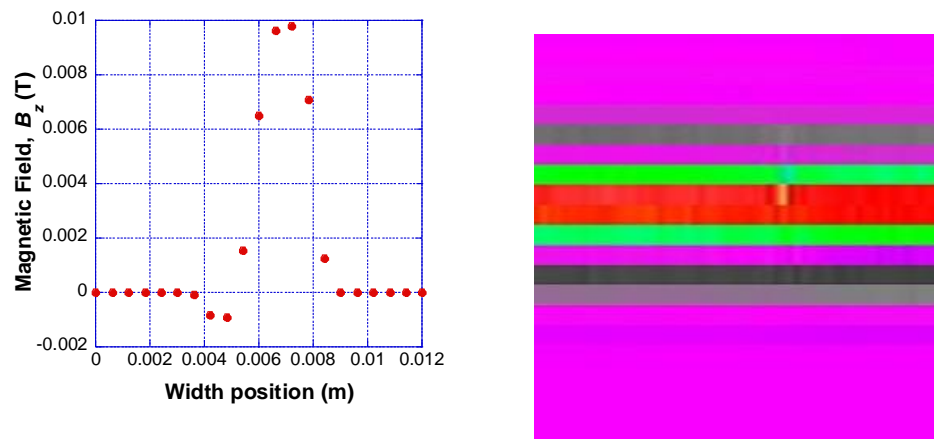

Fig. 6.2 The magnetic field penetration in 1D and 2D

However, by solving the inversion problem of Biot-Savart law, the 2D J_c image does not clearly provide detailed information such as obstacles, as shown in Fig. 6.3. Because of the discrete magnetic field taking from the low resolution of the measurement, the distribution of 2D images is still low spatial resolution.
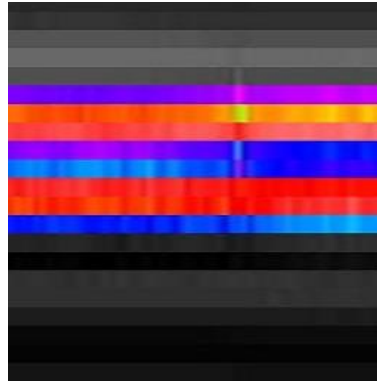

Fig. 6.3 The distribution of critical current density as 2D J_c image

6.2 Interpolation technique for low resolution magnetic image from Tapestar^{TM}

In order to increase the resolution of data taken from Tapestar^{TM}, the Interpolation approach is normally used for constructing the new data points between a range of discrete data points. The interpolation function can be described by the following equation (6.1) [55].

$$y_i = f(x_i) \tag{6.1}$$

Where, $x_i = x_1, x_2, x_3, \ldots, x_n$ is the independent variable values, and $y_i = y_1, y_2, y_3, \ldots, y_n$ is the dependent variable values. The main types of interpolation were divided into three approaches: nearest neighbor, linear, and spline interpolation. The example of these interpolation results is shown in Fig. 6.4. Nearest interpolation takes the nearest data value for each position to be interpolated. The linear interpolation y_i on the line segment connects the two points. These two simply interpolations are still not close to the data in the case of different curves, whereas the spline interpolation performs well with a smaller error.
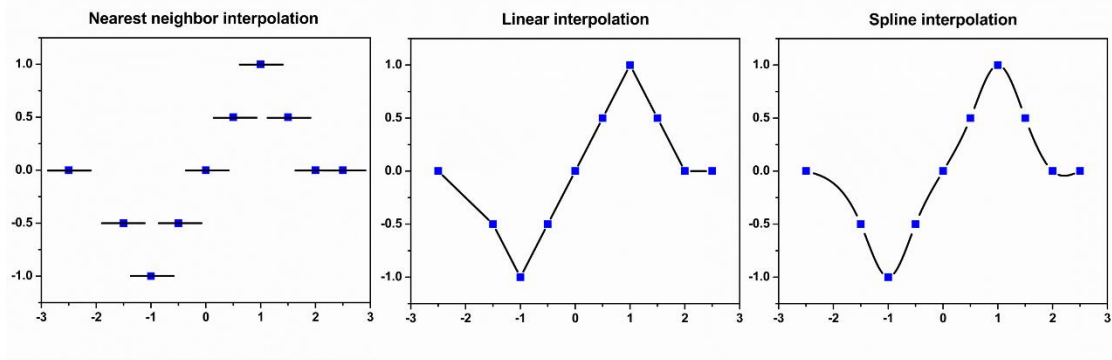
Fig. 6.4 The different interpolation methods

Due to the dependent variable value passing the different curves of the data point based on the third-order polynomial between two adjacent points, the function is defined by the following equation.

$$y_i = f(x_i) = ax_i^3 + bx_i^2 + cx_i + d, \ \ for \ \ (i = 1 \ to \ n) \tag{6.2}$$

where *a, b, c,* and *d* are real numbers and *i* = data points

In this study, we adopted the spline interpolation to the original magnetic data in order to generate a high-resolution image for image analysis. The enhancement result for Tapestar^{TM} results is shown in Fig. 6.5, indicating an increase in data points for original magnetic field gradients by interpolation technique as well as resulting in the more detailed information on magnetic and critical current density images, as shown in Fig. 6.6.

Based on this approach, the interpolation image can be used for the image analysis, such as object detection, as shown in Fig 6.7(a), and the position of the obstacle shows good agreement with the high resolution of J_c image obtained from the RTR-SHPM in Fig 6.7(b). As a result, even though Tapestar^{TM} has a limited number of channels resulting in a lack of more detailed information, we can improve the resolution of the magnetic image and apply it to defect recognition.
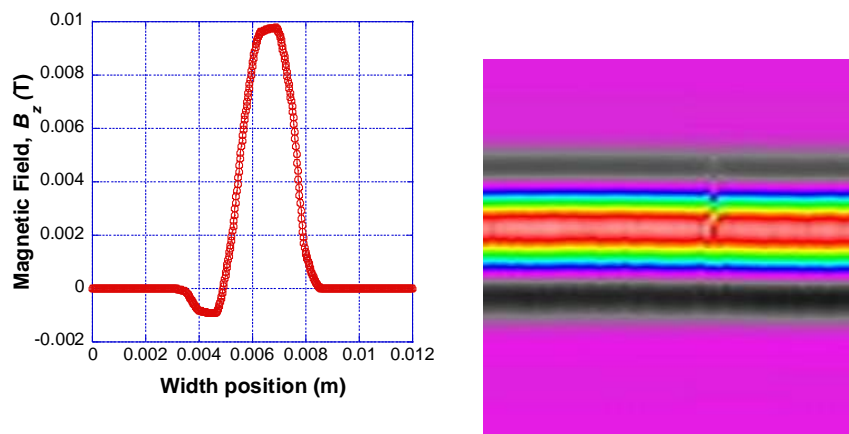
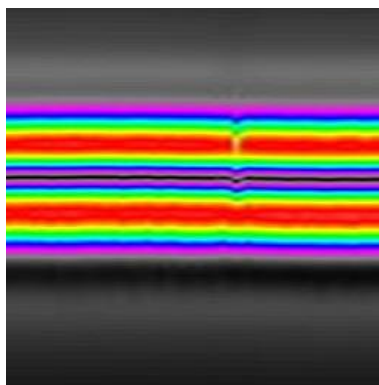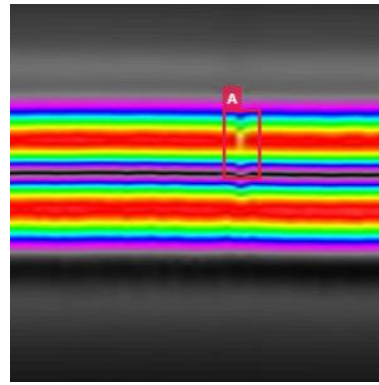Fig. 6.5 The magnetic field penetration in 1D and 2D after interpolating
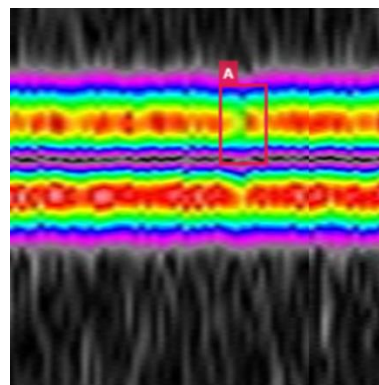

Fig. 6.6 The 2D J_c mapping image after interpolating

(a)

(b)

Fig. 6.7 Example of defect detection result (a) the interpolated J_c image as input, and (b) J_c mapping image obtained RTR-SHPM

Chapter 7

Conclusion

Nowadays, the high-temperature superconducting CCs play an important role in many applications due to their superior high current carrying capability under high magnetic fields. The uniformity of local I_c along the long length tapes is required for improving their practical performance because the local obstacles originated in tapes resulting in degradation I_c. Therefore, characterization is essential to analyze and develop the tapes.

In chapter 1, the general background information and the purpose of this research are discussed. We introduced the critical issue of the HTS tapes due to obstacles and requirements to improve the high performance of practical applications. The instant characterization or analytical techniques is essential for the evaluation and provide such helpful information back to the improvement of the REBCO. Not only merely the critical current, I_c value, but also more advanced information of obstacles is required for the research and development. Based on our remarkable high-resolution 2D characterization: RTR-SHPM, it provides the 2D J_c mapping along the tapes, which is used for visualizing the local defects. Thus, we introduced the deep learning approach based on image analysis such as classification and object detection used in this research. They were integrated with RTR-SHPM for automatically evaluating more detailed information on local obstacles in the long length CCs.

In chapter 2, the principle of two characterization methods to estimate the longitudinal distribution of the critical current, which is a basic indicator for characterizing long superconductors was described. Firstly, the 1D characterization method known as Tapestar^{TM} system is used to estimate the I_c variation in the longitudinal direction as a de facto standard method. Secondly, the 2D characterization method, RTR-SHPM, is used for visualizing 2D inhomogeneity with high spatial resolution measurements across the width direction as well as the longitudinal direction and main characterization generating the 2D image for image analysis in this research.

In chapter 3, with the image classification, we successfully build the reasonable first classification model using critical eight defect images at low I_c region, defined by

extrinsic mechanism and normal images selected at higher average I_c region. The model was able to distinguish more critical defect regions from the normal region, even at the high I_c region throughout 4000 images along the 200-m long CC. Moreover, Using the confidence score for evaluation of correct classification, It presented that the confidence score increases as the $I_{c,min}$ decreases in the defect category, whereas the normal category has a high confidence value as the $I_{c,min}$ increases, and the crossover point is around $I_{c,min} = 260$ A. It is very reasonable because local obstacles will suppress the $I_{c,min}$, and correspond to a set of images that we train the model.

In chapter 4, we further improve the classification model by using the group of defect images categorized as normal with low confidence scores. As a result, the number of defect images was almost 2.5 times more than the previous model. It indicates that smaller obstacles at I_c drops at high values were still the existence, and an increase in the number of training data with critical defect images could improve much more performance of correctness. The image classification was developed to categorize the defect sizes based on different criterions. As the result, we can categorize and estimate defect sizes into three categories: large, medium, and small, based on training size criterions compared to prevision binary classification. Moreover, the classification was extended to different HTS tapes to extract valuable information on local current limiting factors such as the types of local obstacles in each coated conductor tape made from different techniques, influence of fabrication processes so that the properties can be estimated based on this approach.

Based on previous classification results, the model successfully classified the defect region and types of defects. However, it still does not clearly understand the defect size distraction, position, and statistical behavior of its obstacles. Hence, in chapter 5, we adopted the deep learning-based object detection to the RTR-SHPM to extract more advanced factors. This method allows us to obtain the size, clearly understand the influence of the defect region on ΔI_c due to suppressing of I_c in its defect regions and indicate the occurrence of the defects following Fractal behavior. Moreover, the distribution of defect size obtained from multi-classification results was confirm that defects categorized in large and medium sizes coincide with the object detection results because such a small size is not suppressed I_c significantly, which the smallest size is around 5 mm in the case of object detection results

Lastly, in chapter 6, with the 1D characterization method, Tapestar^{TM} system could generate the 2D images that were still low-resolution images. We applied the interpolation technique to original Tapestar^{TM} data for enhancing the 2D images. As a result, the enhanced image showing the more detailed information was able to be applied to image analysis.

One of the important issues for introducing DL based image analysis for the defect detection is the imbalanced training data sets because the frequency of defects becomes less in recent practical REBCO tapes. As adopted in this study, pre-trained high performance such as GoogleNet can solve this issue to some extent. However, the classification performance could actually be improved further if we increased the input defect images for training based on the first model. The threshold (or confidence) value for the category may also be influenced by such imbalanced input data as discussed in Chapter 4. The influence of the imbalanced dataset on the precision of the classification is not yet fully understood in this study and the method to increase the training datasets for defect images need to be studied further as a future task. Even though, by applying DL based image recognition, we have succeeded in clarifying how much defect size will influence the local I_c drop larger than the intrinsic fluctuation, and their statistical nature, also we could reveal process dependent defect images by comparing difference processes. Those insights give us much more rich information on the current limiting mechanisms of the REBCO tapes and can lead to the improvement of process conditions. Such feedback must have a huge impact not only on characterization methodology but also on materials development.

References

[1]   H. K. Onnes, "The resistance of pure mercury at helium temperatures," *Commun. Phys. Lab. Univ. Leiden,* vol.12, p.120, 1911.

[2]   C. Kittel, *Introduction to Solid State Physics.* 8th ed. New York: John Wiley & Sons, 2004.

[3]   J. G. Bednorz, K. A. Mueller, Possible high T_C superconductivity in the Ba-La-Cu-O system, *Zeitschrift für Physik B,* vol. 64, 1986, 189–193.

[4]   C. W. Chu, P. H. Hor, R. L. Meng, L. Gao, Z. J. Huang, and Y. Q. Wang, "Evidence for Superconductivity above 40 K in the La-Ba-Cu-0 Compound System*," Phys. Rev. Lett.* vol. 58, no. 4, *1987, 405*-407.

[5]   H. Maeda, Y. Tanaka, M. Fukutumi, T. Asano, "A New High-T_c Oxide Superconductor without a Rare Earth Element". *Japanese Journal of Applied Physics*, Vol. 27, No. 2, 1988,209-210.

[6]   B.H. Annette, and K. Hugo, "High-temperature superconductors: underlying physics and applications," *Z. Naturforsch.,* 2019

[7]   M. Igarashi, C. Tashita, T. Hayashida*, et al.,* "RE123 Coated Conductors," *Fujikura Technical Review*, 2009.

[8]   A. Mogro-Campero, L. G. Turner, and E. L. Hall, "Large differences of critical current density in thin films of superconducting YBa$_2$Cu$_3$O$_{7-x}$," *J. Appl. Phys.,* Vol. 65, No. 12, 15 June 1989.

[9]   M.P. Paranthaman, and T. Izumi, "High-performance YBCO-coated superconductor wires. *MRS Bull,* Vol. 29, No. 8, 2004, 533–541.

[10]   Y. Iijima, K. Onabe, N. Futaki, et al., "Structural and transport properties of biaxially aligned YBa$_2$Cu$_3$O$_{7-x}$ films on polycrystalline Ni-based alloy with ion-beam-modified buffer layers," *J Appl Phys.* Vol 74, No. 3, 1993, 1905–1911.

[11]   A. Goyal, D.P. Norton, J. D. Budai, et al., "High critical current density superconducting tapes by epitaxial deposition of YBa$_2$Cu$_3$O$_x$ thick films on biaxially textured metals," *Appl Phys Lett. Vol.,* 69, No. 12, 1996, 1795–1797.

[12]   Superconducting Bachelor thesis Seminar Material (Chapter 4), Takanobu Kisu (Kyushu Univ.)

[13]   Y. Iijima, N. Tanabe, O. Kohno, et al., "In-plane aligned YBa/sub 2/Cu/sub 3/O/sub 7-x/ thin films deposited on polycrystalline metallic substrates," *Appl. Phys.Lett.,* Vol.60, 1992,769-771.

[14]   IBAD process, [Online]. Available:<http://www.istec.or.jp/>.

[15]   A. P. Malozemoff, S. Fleshler, M. Rupich, *et al.,* "Progress in high temperature superconductor coated conductors and their applications*," Supercond. Sci. Technol.,* 2008.

[16]   V. Selvamanickam, G.B. Galinski, G. Carota, et al., "High-current Y–Ba–Cu–O superconducting films by metal organic chemical vapor deposition on flexible metal substrates," *Physica C,* 2000.

[17]   M. Igarashi, K. Kakimoto, S. Hanyu, et al., "Remarkable progress in fabricating RE123 coated conductors by IBAD/PLD technique at Fujikura," *Journal of Physics: Conference Series,* 2010.

[18]   V. Matias, J. Rowley, Y. Coulter, *et al.,* "YBCO films grown by reactive co-evaporation on simplified IBAD-MgO coated conductor templates," *Supercond. Sci.* Technol. 2010.

[19]   Y. Iijima, The 5th Asian Superconductivity school, 2nd Lecture, 2021

[20]   Adir Moyses Luiz, Overview of Possible Applications of High T_c Superconductors, Applications of High T_c Superconductivity, Dr. Adir Luiz (Ed.), 2011.

[21]   RE-based HTS wire, [Online]. Available:<http://www.fujikura.co.jp/>.

[22]   T. Masuda, H. Yumura, M. Watanabe, "Recent progress of HTS cable project," *Physica C*, Vol. 468, 2008, 2014–2017.

[23]   MRI system, [Online]. Available: <https://www.trademed.com/ products /6198 /MRI-System.html>.

[24]   The L0 series Maglev at Yamanashi test track in Japan, image: Saruno Hirobano, [Online]. Available: <https://www.railtech.com/rolling-stock/2022/03/29/the-journey-of-the-maglev-train/>.

[25]   Nuclear fusion power, [Online]. Available :<https://physicsworld.com/a/ europe-beats-japan-to-iter-prize/>.

[26]   S. S Oh, H.S Kim, D.W Ha, H.S Ha, K. Sim, and H.S Shin, "Variation of local critical current due to mechanical strain in RCE-REBCO coated conductors," *IEEE Trans. Appl. Supercond.*, vol. 24, no. 3, Jun. 2014, Art. no. 6900204.

[27]   K. Higashikawa, M. Inoue, S. Ye, A. Matsumoto, H. Kumakura, R. Yoshida, and T. Kiss, "Scanning Hall-probe microscopy for site-specific observation of microstructure in superconducting wires and tapes for the clarification of their performance bottlenecks," *Supercond. Sci. Technol*., vol. 33, no. 6, 2020, Art. no. 064005.

[28] M. Friesen and A. Gurevich, "Nonlinear transport current flow in superconductors with restricted geometries," *Phys. Rev. B*, vol. 63, p. 064521, 2001.

[29] S. Furtner, R. Nemetschek, R. Semerad, G. Sigl, and W. Prusseit, "Reel-to-reel critical current measurement of coated conductors," *Supercond. Sci. Technol.*, vol. 17, 2004, pp. 281-284.

[30] K. Higashikawa, *et al.,* "Scanning hall-probe microscopy system for two-dimensional imaging of critical current density in RE-123 coated conductors," *Phys. C, Supercond. Appl.,* vol. 471, pp. 1036–1040, 2011.

[31] K. Higashikawa, K. Katahira, K. Okumura *et al.,* "Lateral distribution of critical current density in coated conductors slit by different cutting methods", *IEEE Trans. Appl. Supercond.*, vol. 23, no. 3, Jun. 2013, 6602704.

[32] M. Igarashi, K. Kakimoto, S. Hanyu, et al., "Advanced development of IBAD/PLD coated conductors at FUJIKURA," *Physics Procedia*, Vol. 36, 2012, 1412-1416.

[33] B. Roter, and S. V. Dordevic, "Predicting new superconductors and their critical temperatures using machine learning," Phys. C: Supercond. Appl., vol. 575, 2020.

[34] A. A. Moghaddam, "Image processing techniques for classification of linear welding defects," 2nd International Conference on Knowledge-Based Engineering and Innovation (KBEI), 2015.

[35] L. Jiao, F. Zhang, F. Liu, S. Yang, *et al.,* "A survey of deep learning-based object detection," *IEEE Access*, vol 7, 2019, pp. 128837 – 128868.

[36] K. Higashikawa *et al.,* Characterization of local J_c distribution in Superconducting wires and tapes based on Scanning Hall probe microscopy Vol.49, No.9, pp.485-493, 2014.10.

[37] Bradley J. Roth et al: "Using a magnetometer to image a two-dimensional current distribution", Journal of Applied Physics, Vol. 65, No. 1, 1989, 361-372.

[38] THEVA[Online]. Available:< http://theva.com/ >.

[39] H. Simon, Neural networks and learning machines 3rd ed. 2009.

[40] Aurélien Géron, Hands-On Machine Learning with Scikit-Learn and TensorFlow, 2017.

[41] C. Szegedy, W. Liu, Y. Jia, *et al.,* "Going Deeper with Convolutions," *IEEE Conference on Computer Vision and Pattern Recognition,"* 2015.

[42] Convolutional Neural Networks, [Online]. Available:<https://www.ibm.com/>.

[43]   D. Quintero, B. He, B. C. Faria, A. Jara, C. Parsons, S. Tsukamoto, R. Wale et al., IBM PowerAI: Deep Learning Unleashed on IBM Power Systems Servers.IBM Redbooks, 2019.

[44]   IBM, PowerAI Vision. "PowerAI Vision Guide." [Online]. Available: <https://www.ibm.com/docs/en/SSRU69_1.1.4/base/vision_pdf.pdf >.

[45]   T. Kiss, M. Inoue, T. Shoyama, S. Koyanagi, D. Mitsui, T. Nakamura, K. Imamura, A. Ibi, Y. Yamada, T. Kato, T. Hirayama, and Y. Shiohara, "Visualizing transport properties in IBAD based YBCO coated conductors by multiple analysis techniques", *IEEE Transactions on Applied Superconductivity*, vol. 17, no. 2, Jun 2007, pp. 3211-3214.

[46]   M. Hossin, and M.N Sulaiman. (2015). "A review on evaluation metrics for data classification evaluations," *International Journal of Data Mining & Knowledge Management Process,* vol. 5, no. 2, 2015.

[47]   R. R. Selvaraju, *et al.,* "Grad-cam: Visual explanations from deep networks via gradient-based localization," *The IEEE International Conference on Computer Vision (ICCV)*, 2017, pp. 618-626.

[48]   I. Sutedja, *et al.,* "Imbalanced data classification using auxiliary classifier generative adversarial networks," *International Journal of Advanced Trends in Computer Science and Engineering,* vol. 9, no. 2, 2020.

[49]   A. D. Sharanya, *et al.,* "Transfer-learning for differentiating epileptic patients who respond to treatment based on chronic ambulatory ECoG data," *9th International IEEE EMBS Conference on Neural Engineering San Francisco, CA, USA,* 2019.

[50]   Mark S. Nixon and Alberto S. Aguado. "Feature extraction and image processing", Academic Press, 2008, p. 88.

[51]   L. Jiao, F. Zhang, F. Liu, S. Yang, *et al.,* "A survey of deep learning-based object detection," *IEEE Access*, vol 7, 2019, pp. 128837 – 128868.

[52]   C. Lee, H. J. Kim, and K. W. Oh, "Comparison of faster R-CNN models for object detection," *16th International Conference on Control, Automation and Systems (ICCAS 2016)* ,2016.

[53]   C. L. Zitnick and P. Dollar, "Edge boxes: locating object proposals from edges," *European Conference on Computer Vision*, 2014.

[54]   T. Kiss, M. Inoue, K. Higashikawa *et al.,* "Comparison between Bi-2223 tape and RE-123 coated conductor from the view point of current transport properties influencing thermal stability," *Cryogenics*, vol. *80*, 2016, pp. 221-228.

[55]   K. Wang, *et al.,* "A study of cubic spline interpolation," *Insight. Rivier Academic Journal,* vol. 9, no. 2, 2013.

Acknowledgements

Lastly, I would like to express my gratitude to my family for their love, encouragement, and generous support throughout my life. I can not reach my goal and success without them.

Natthawirot Somjaijaroen